

# Unified theory of bound and scattering molecular Rydberg states as quantum maps

Barbara Dietz<sup>a,d</sup> Maurice Lombardi<sup>b,d,\*</sup>  
Thomas H. Seligman<sup>c,d</sup>

<sup>a</sup>*Institute for Nuclear Physics. Technische Universitat Darmstadt.  
Schlossgartenstrasse 9. Darmstadt. Germany*

<sup>b</sup>*Laboratoire de Spectrométrie Physique(CNRS UMR 5588), Université  
Joseph-Fourier de Grenoble, BP87, F-38402 Saint Martin d'Hères Cédex, France*

<sup>c</sup>*Centro de Ciencias Físicas, UNAM, Av. Universidad s/n, Col. Chamilpa,  
Morelos, Mexico*

<sup>d</sup>*Centro Internacional de Ciencias, Cuernavaca, Mexico*

---

## Abstract

Using a representation of multichannel quantum defect theory in terms of a quantum Poincaré map for bound Rydberg molecules, we apply Jung's scattering map to derive a generalized quantum map, that includes the continuum. We show, that this representation not only simplifies the understanding of the method, but moreover produces considerable numerical advantages. Finally we show under what circumstances the usual semi-classical approximations yield satisfactory results. In particular we see that singularities that cause problems in semi-classics are irrelevant to the quantum map.

*Key words:* Rydberg molecule, Semi classical physics, Quantum chaos  
*PACS:* 5.45.Mt, 03.65.Sq, 31.15.Gy, 33.80.Rv, 34.80.Gs

---

## 1 Introduction

Electronic states of molecules are called Rydberg states, as opposed to valence states (whether covalent or ionically bound), when an outer electron moves far

---

\* Corresponding author. Fax: +33 476 635 495

*Email addresses:* dietz@linux6.ikp.physik.tu-darmstadt.de (Barbara Dietz), Maurice.Lombardi@ujf-grenoble.fr (Maurice Lombardi), seligman@ce.fis.unam.mx (Thomas H. Seligman).

away from the remaining ionic core. These states form electronic series which converge towards the ionization limit of the molecule.

The starting point of the quantum analysis of such states was the Quantum Defect Theory (see e.g. the review article by Seaton [1]), established first for atoms. It was shown that, due to the non zero spatial extension of the ionic core, the levels near the ionization limit follow the hydrogenic Rydberg law  $E_n = -\text{Ry}/(n+d)^2$ , with only a constant (or nearly so) shift  $d$  of the principal quantum number  $n$ , entitled Quantum Defect. Quantum Defect Theory was extended to a Multichannel Quantum Defect Theory (MQDT), for the case that there are several series which converge to nearby states of the ion, and interact strongly. It was shown that MQDT gives a unified theory of bound states, autoionizing states and electron-ion scattering cross sections. This theory depends only on a small number of parameters, basically one quantum defect per interacting series. Practically, all is solved with matrices whose size is the number of series, while “brute force” methods would in principle try to diagonalize a matrix which contains an infinite number of levels for each series.

This theory was extended to molecules by Fano [2,3]. There are always many interacting series corresponding to the rotational states of the ionic core. Indeed the slow velocity of the core rotation leads to a splitting of the rotational states of the core which is of the same order of magnitude as the splitting between high lying electronic Rydberg states. The novelty were the implications of the anisotropy of the core. The effect of this anisotropy on the ionic potential decays faster with distance  $r$  than the point charge  $1/r$  Coulomb potential, at least as  $1/r^2$  or  $1/r^3$ . Fano showed that the key point of the analysis is the existence of a cut off distance  $r_0$ . Below this distance the motion of the outer electron is tightly bound to the *direction* of the ionic core, above it the two become independent. Many detailed studies have followed on moderately excited Rydberg states of molecules, see e.g. reviews in refs. [4,5].

A novelty resulting from the studies of very high lying states of molecular Rydberg series was the experimental observation of “clear zones” in such interacting series. It was soon understood that this so called “stroboscopic effect” corresponds to resonances between the period of rotation of the core and the period of the outer electron orbit [6,7]. In order to study the relationship of this phenomenon with classical and quantum chaos, the classical limit of the MQDT theory was established [8]. A Poincaré surface of section was introduced, whose coordinates correspond to parameters of the molecular system when the electron leaves the sphere of radius  $r_0$ . The studies showed that the “stroboscopic effect” corresponds to a periodic reestablishment of a nearly integrable phase space structure at each resonance, while the classical phase space is completely chaotic in between.

The impetus for the present study was given by papers of Bogomolny where he introduces a semi-classical method for the quantization of a classical Poincaré surface of section Map (PM) [9,10,11], and some other follow up papers, e.g. [12]. The original semi-classical method is not unique and is prone to singularity problems, thereby raising the question about its relationship with a true quantization. We followed exactly the opposite route, starting from a purely quantum method (MQDT), establishing its classical limit, and at last studying Poincaré surfaces of sections. Our system is ideal for the study of this problem because we know in advance the correct result. Furthermore our system has an unusual and non trivial geometry, the *phase space* being a sphere. For bound systems, a preliminary report of the interpretation of MQDT as a Quantum Poincaré Map (QPM) was provided in ref. [13]. However, the relationship with the theory of Bogomolny was only a formal analogy of the final quantum and semi-classical formulae used to compute the levels. In this paper we study and compare step by step classical, semi-classical and quantum descriptions of the same system.

Another important property of the MQDT is, that it describes bound and ionized states in a unified way. Hence, we may use it to study the quantization of the so called Jung Scattering Map (JSM) for ionized states [14]. Indeed Jung proposed to send back ionizing trajectories onto the molecule in a well prescribed way, in order to obtain a compactification of the phase space for above threshold states. The role of the JSM in this context, has been touched upon previously to elucidate certain properties of the *S*-matrix [15]. In the light of the reinterpretation of MQDT as a QPM for bound systems it seems very attractive to attempt a comprehensive description, which extends the advantages outlined in ref. [13] to include both scattering, bound states and resonances.

The purpose of this paper is to present a classical map which combines the PM for the part of the phase space corresponding to negative energies of the excited electron with the JSM for the positive energy region, and then to interpret MQDT as the quantization of the resulting symplectic map. This will provide basically two advantages. On one hand a conceptual advantage, as the method and its approximation can be formulated in the context of a classical map and its subsequent quantization. In particular, we will see that phase space representations of wavefunctions for open channels quantize on trajectories of the JSM in the same way as bound states and ionization resonances quantize on trajectories of the PM. On the other hand on a more practical level, the dynamics is shown to be semi-separable [12,16] which permits a decomposition into separable steps, and suggests to choose a surface of section such that it separates these steps. Consequently, the QPM for half an evolution step of the system contains the relevant information, and its diagonalization will permit to find eigenvalues, eigenvectors, the level dynamics, *etc* in a simplified way. This will be particularly useful when dealing with near degenerate levels or

resonances which occur frequently and cause considerable difficulties in the conventional approach [13,17].

In the next section we shall develop the generalized classical PM, which includes the JSM for the particular conditions of a Rydberg molecule. In the third section we shall present the main result of this paper. MQDT for bound states and open systems will be formulated as a generalized QPM. In both these sections attention will be given to relaxing the common approximation to keep the absolute value of the electron angular momentum fixed. In section four we shall discuss applications and show numerical examples that demonstrate the practical advantages of this method and may also give some new insight in situations of quantum chaotic scattering. These examples will exclusively be given within the approximation of fixed absolute value of the electron angular momentum, mainly to show nice two dimensional plots of surfaces of section. As the QPM was originally proposed in a semi-classical approximation [9,10,11], we shall in section 5 compare the approximate results of semi-classics to the ones of the "exact" QPM. We shall see that singularities causing problems in semi-classics are absent in the QPM. Therefore the QPM can be used to test regularization procedures for semi-classics.

## 2 Generalized classical Poincaré map for Rydberg molecules

### 2.1 Principle

A Rydberg molecule is composed of an ionic positively charged molecular core and an outer electron. It is specifically given the name "Rydberg" when one considers states just below or above the ionization threshold, where the outer electron performs large excursions far away from the core. This situation allows to define a distance  $r_0$  which separates the potential felt by the outer electron into a long range Coulomb part, and a short range or collision part. In the long range part, the outer electron only feels the spherically symmetric  $-1/r$  Coulomb potential of the core (we use throughout the "atomic units" (a.u.)  $e = \hbar = m = 1$ ). Its motion is comparatively slow because one considers states near the ionization limit, but it can be either bound or unbound. The electron moves along a Kepler orbit whose plane and axis are fixed in the laboratory frame. Meanwhile, the ionic core rotates freely around its angular momentum  $\mathbf{N}$ . In the collision area the electron feels the lower symmetry, faster decreasing, part of the potential of the core (dipolar ( $\propto 1/r^2$ ) or quadrupolar ( $\propto 1/r^3$ ) for a diatomic molecule) and it is strongly accelerated. This strong acceleration leads to a short range collision motion, which is approximately the same for a total energy slightly below or above the ionization threshold, since the difference between the corresponding velocities is negli-

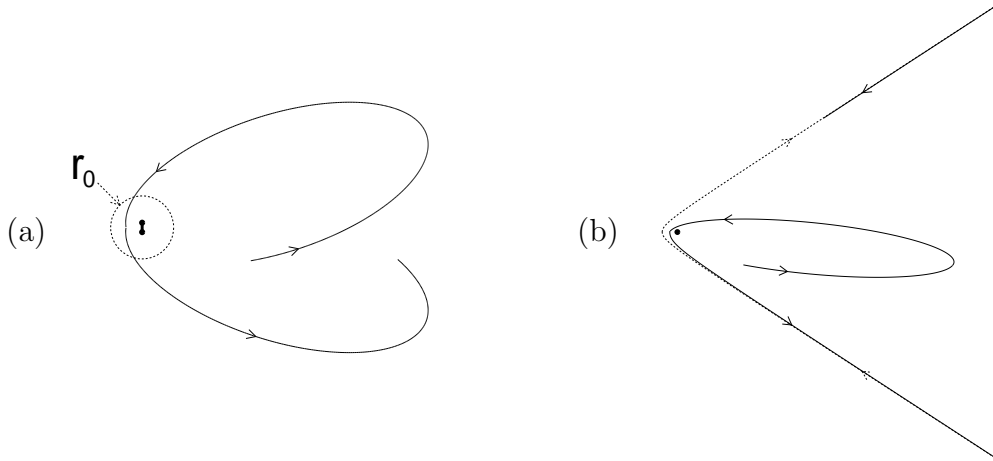


Fig. 1. (a) The outer electron follows a Kepler orbit, fixed in space, for large distances  $r > r_0$  and changes the Kepler orbit for  $r < r_0$  by interaction with the short range part of the ionic core potential. (b) When the electron ionizes the Jung’s recipe is to feed back the electron which escapes to infinity by doing a step backwards in time without collision with the core (i.e. a pure Kepler hyperbola with reverted velocity), and then re launch the electron towards the molecule along the resulting asymptotic trajectory for the next collision.

ble compared to the velocity produced by the acceleration. This is basically the reason why in quantum mechanics MQDT treats bound and unbound states in a unified way. During the collision there is exchange both of angular momentum and energy between the electron and the core. The exchange of angular momentum implies a change of the plane of the Kepler orbit, since the angular momentum of the electron  $\mathbf{L}$  is perpendicular to its plane (Fig. 1(a)). The exchange of energy leads to a variation of the eccentricity of the orbit, and may turn it into an ionizing trajectory. In this case the Jung’s recipe [14] is to feed back the electron which escapes to infinity by doing a step backwards in time without collision with the core (i.e. a pure Coulomb step with reverted velocity), and then re launch the electron towards the molecule along the resulting asymptotic trajectory (Fig. 1(b)). By doing this, one obtains trajectories which cross infinitely many times the  $r = r_0$  sphere. Poincaré surfaces of section are described by a set of parameters of the molecular system at those instants where the electron crosses outwards the sphere. To define these parameters (several sets are possible) we first need to define precisely the reference frames and count the number of independent parameters for the determination of the dimension of this Poincaré surface of section.

## 2.2 Reference frames

In this work, we will use three reference frames, the laboratory frame and two molecular reference frames, entitled “quantum” and “classical” reference frames. They are shown in Fig. 2.

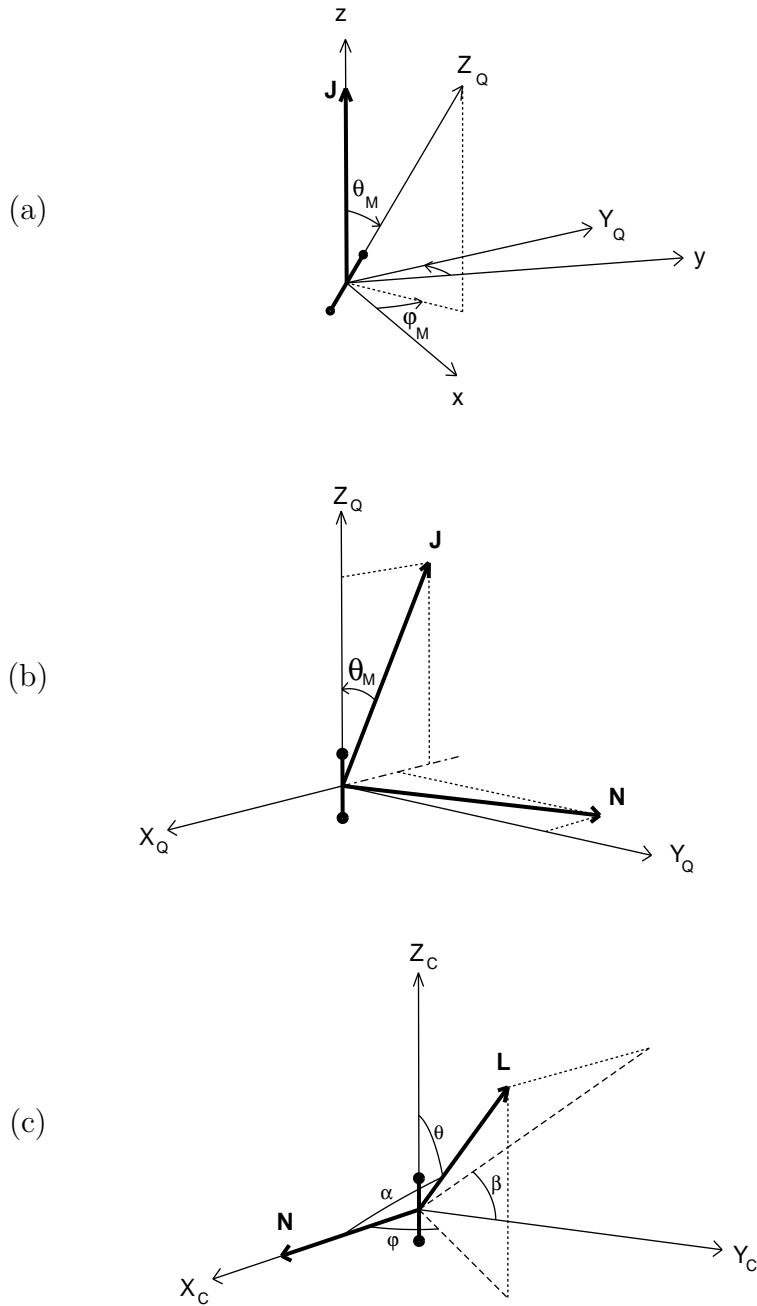


Fig. 2. Reference frames for the molecular system. (a) Laboratory frame. Its  $Oz$  axis is selected along the total angular momentum  $\mathbf{J}$  (b) “Quantum” molecular reference frame. Obtained from the laboratory frame with a rotation of Euler angles  $\varphi_M, \theta_M, 0$ . Its  $OZ_Q$  axis is along the molecular axis  $\hat{\mathbf{M}}$ . (c) “Classical” molecular reference frame. It is obtained from the “quantum” by a rotation around  $\hat{\mathbf{M}}$  which brings the  $OX_C$  axis along the angular momentum  $\mathbf{N}$  of the core. This frame is physically the most significant, and all other figures of this paper are drawn with this convention.

- (a) Laboratory frame. Due to the global rotational invariance which entails conservation of the total angular momentum  $\mathbf{J}$ , we can select, without loss of generality, its  $Oz$  axis along the total angular momentum  $\mathbf{J}$ . The other two axis are arbitrary (but fixed). In this frame the axis  $\hat{\mathbf{M}}$  of the core has (varying) polar angles  $\theta_M$  and  $\phi_M$ .
- (b) “Quantum” molecular reference frame. It is obtained by a rotation of the laboratory frame by the Euler angles  $\theta_M, \varphi_M, 0$  (as common in quantum mechanics [18] we use the y convention for the Euler angles [19, Appendix B]). We entitled it “quantum” because it is the frame used in the quantum theory of molecules. The third Euler angle is arbitrary for a diatomic molecule, and is sometimes selected as  $\pi/2$  [20] for normalization reasons, which do not concern us here. Therefore, we prefer to stick to the conventions of the first paper by Fano [2]. We restrict to the diatomic case for simplicity, a third Euler angle would be necessary for a polyatomic core. In this frame  $\mathbf{J}$  lies in the “vertical” plane  $OX_QY_Q$ . The angular momentum of the core  $\mathbf{N}$  for a diatomic molecule is perpendicular to the core axis  $\hat{\mathbf{M}}$ , because the moment of inertia of the core around it is zero. It is thus in the “horizontal” plane  $OX_QY_Q$ .
- (c) “Classical” molecular reference frame. This frame is obtained from the “quantum” frame by a rotation around  $OZ_Q = OZ_C$  such that the new  $OX_C$  axis is along  $\mathbf{N}$ . As will become obvious below, from the physical point of view this frame is the most appropriate for the visualization of the results. As in previous publications [8,13,15,17,21] we will use it in all figures of this paper.

Formulas to go from one reference frame to the others are obtained from simple geometric arguments based on the previous remarks, and are established in Appendix A.

### 2.3 Count of parameters and the dimension of the Poincaré surface of section

The configuration space is described by five coordinates in the laboratory frame. Two angles  $\theta_M, \varphi_M$  describe the position of the axis of the diatomic ionic core (a third would be necessary for a polyatomic core). Two angles  $\theta_e, \varphi_e$  and a radial distance  $r$  describe the position of the electron. Thus configuration space has a dimension of five and phase space has a dimension of ten. Conservation of the total angular momentum  $\mathbf{J}$  reduces the dimension of phase space by 4, two for the Poisson commuting actions  $J_z$  and  $J^2$ , and two for the associated angles. The first angle can be selected as the polar angle  $\varphi_J$  associated with  $J_z$ , that is the angle of the projection of  $\mathbf{J}$  onto the laboratory plane  $Oxy$ , which is constant (with our choice of the laboratory axis it is in fact undetermined but this is of no importance). The second can be a global rotation angle around  $\mathbf{J}$  associated to  $J^2$ , which is cyclic (but not

constant): see e.g. the analogous reduction to the  $\{j_1, j_2, j_3, w_1, w_2, w_3\}$  action angle system for the pure Kepler problem in [19, Chap. 10-7]. Consequently, the dimension of the reduced phase space in the general case is six, and a Poincaré surface of section has dimension four.

The introduction of the auxiliary approximation that the modulus  $L$  of the angular momentum  $\mathbf{L}$  of the electron is conserved during the collision reduces the dimension of the phase space by two ( $L^2$  and the associated angle), and thus the Poincaré surface of section has dimension two, which enables graphical representations. This approximation was used in our previous works [8,13,15,17,21], and is valid in the experimental works which motivated the theoretical study [6,7]. The reason for its validity is that the splitting between different electronic  $L^2$  levels produced by the spherically symmetric part of the potential of the core is much larger than the splitting between sub levels of  $L^2$ , produced by its anisotropic part. In the experiments,  $L$  takes low values, restricted to 0...2 by a two steps laser excitation. Here, however we want to study the semi classical limit, where the angular momenta take large values. There are two possibilities to increase angular momenta. First we can increase them without changing other molecular parameters. This is experimentally possible since the application of R.F. fields [22] or of combined electric and magnetic fields [23] in atomic Rydberg states enable to climb the  $L$  ladder up to circular orbits. In this case the constant  $L$  approximation breaks down for higher  $L$ . A study of the consequences for this case has been performed in ref. [24]. However, this is not what we aim at, since it implies a complete change of the physics of the problem at hand. We want to gain insight into the physics of the experimental works in refs. [6,7], by establishing its semi-classical limit. Mathematically this amounts to letting  $\hbar \rightarrow 0$  while keeping all classical parameters constant. Practically, since  $\hbar$  is a constant of nature (taken as 1 in atomic units), this requires the increase of all classical parameters while keeping constant their dimensionless ratios. For example, decreasing  $\hbar$  by a factor of  $m$  implies to multiplication of all momenta by  $m$ , angular  $L$ ,  $J$ ,  $N$ , and principal,  $n$ . The Kepler period  $T_e$  of the orbital motion of the electron, which is proportional to  $n^3$  is thus multiplied by  $m^3$ , the period  $T_N$  of the rotational motion of the core which is proportional to  $I/N$  (where  $I$  is the moment of inertia of the core) must be multiplied by the same factor, so that  $I$  scales as  $m^4$ . Similarly, one must scale the ratio between the geometric size of the core and the De Broglie wavelength, keeping constant the core's shape parameters (ratio anisotropic / isotropic). This maintains constant the ratio of the classical periods associated with  $L$ , due to the isotropic part of the short range potential, and with  $\Lambda = \mathbf{L} \cdot \hat{\mathbf{M}}$ , due to the torque produced by the anisotropic part of this short range potential. This maintains the validity of the approximation of constant  $L$ . Of course this needs proportionally larger molecules, more difficult experimentally to deal with, but not completely out of reach since recent experimental studies have found Rydberg states on molecules as large as Benzene Argon complexes [25], Diazacyclooctane (DABCO) and bis

(benzene) chromium (BBC) [26].

Thus, for practical reasons, we shall continue to use the constant  $L$  approximation in many formulae and all pictures presented in this article. Yet we shall show, especially in the present and the next sections, that these restrictions are not essential for the interpretation of MQDT as a QPM, and how formulae can be generalized.

Finally notice that in ref. [21], we started with only seven parameters. The three missing parameters were the three angles associated to the three conserved momenta  $J^2$ ,  $J_z$  and  $L^2$ . This is legitimate in classical mechanics since they can be computed afterwards by a mere quadrature. For the comparison between classical and quantum mechanics, which is the main purpose of this work, this is natural since these angles are totally undetermined due to Heisenberg's uncertainty principle for well defined values of the corresponding momenta.

#### 2.4 Parameterizations of the Poincaré surface of section

We first discuss the case of constant  $L$ . For a proper parameterization of a two dimensional Poincaré surface of section, we need two conjugated parameters, a momentum and an angle. We will not use the most obvious angles  $\theta_e$ ,  $\varphi_e$  of the electron and their conjugated momenta, but angles associated with angular momenta  $L_{Z_Q}$  of the electron and  $N$  of the core because in the quantum MQDT description of the molecule, these momenta enter naturally as (approximate) quantum numbers for the limiting cases [2]. There are different choices, depending on whether we work in the molecular or the laboratory frame.

- (1) “Quantum” molecular frame. We use the projection  $\Lambda = L_{Z_Q} = \mathbf{L} \cdot \hat{\mathbf{M}}$  of the electron angular momentum onto the core axis, and the angle  $\varphi_L^Q$ , the azimuthal angle of the projection of  $\mathbf{L}$  into the horizontal plane  $OX_QY_Q$ , conjugated like the  $j_1, w_1$  pair in [19, eq. 10-139]. This choice of parameters implies that the Poincaré surface of section is a sphere on which every point is defined by  $\theta_L^Q = \arccos(\Lambda/L)$  and  $\varphi_L^Q$ , i.e. the direction of  $\mathbf{L}$  in the molecular frame.
- (2) Laboratory frame. We use the modulus  $N$  of the angular momentum of the core (not one of its projection onto laboratory frame). Intuitively, the associated angle is the angle of rotation  $\varphi_N$  of the molecular core  $\hat{\mathbf{M}}$  around the direction of  $\mathbf{N}$ , and the only possible reference for this angle is given by the direction of the total angular momentum  $\mathbf{J}$ . A proof of this intuition, namely a precise definition of this angle, formulae relating the pairs  $\{L_{Z_Q}, \varphi_L^Q\}$  and  $\{N, \varphi_N\}$ , and the proof that this transformation

is canonical is given in Appendix A.1.

- (3) “Classical” molecular frame. We use  $L_{Z_C} = L_{Z_Q}$  (the two  $Z$  axis coincide), and  $\varphi_L^C$ , the angle referred to  $N$  in the “horizontal” plane (Fig. 2(c)). Notice that this pair is *not* conjugated, as discussed in section 5.1. The consequence is that the Poincaré map does not conserve the area of the sphere with these coordinates, a small effect for the choice of parameters we have used in this paper. We stick nevertheless to this choice for graphical representations, because it gives more intuitive physical pictures as shown below.

Notice that with this choice of parameters, the direction of the plane of the Kepler orbit is well determined in the molecular frame, since it is perpendicular to  $\mathbf{L}$ , and its eccentricity is well determined by  $L$  and the electron energy  $E_e$ , but that the direction of its main axis in this plane, i.e. the Laplace-Runge-Lenz vector  $\mathbf{A}$  [19], is not. As explained in ref. [8], the reason for this is that no component of  $\mathbf{A}$ , which defines this major axis, commutes with  $L^2$  which is kept fixed. Our counting of parameters implies that the direction of  $\mathbf{A}$  is not an independent parameter.

Introducing the approximation that  $L$  is a constant has as a consequence that the information about the main axis direction is hidden in the angle associated to  $L^2$ . Then, the choice of action angle variables corresponds to that typically used in the pure bound Kepler problem in celestial mechanics [19]. The actions are  $j_1 = L_z$ ,  $j_2 = L$  and  $j_3 = \sqrt{-1/2E_e}$  (i.e. “principal quantum number”). The associated angles are the “longitude of the ascending node”  $\Omega$  ( $= \varphi_L + \pi/2$  with our notations), the “argument of the perihelion”  $\omega$ , which is the direction of the main axis in the orbital plane (or the direction of  $\mathbf{A}$  in this plane) we are looking for, and the “mean anomaly” which is proportional to time. Thus, the angle of the main axis of the ellipse, which is constant for pure Kepler motion, i.e. for Rydberg molecules when the electron is far away from the core, but varies during the collision, is part of the map only, if the approximation  $L^2$  constant is omitted.

### 2.5 Description of the classical Poincaré map

We now briefly describe the PM, both in the laboratory and in the molecular frame. The dynamics is composed of two independent consecutive steps:

- (i) collision step: when  $r \ll r_0$  the electron feels the short range anisotropic part of the potential. We suppose that this step is very short, so that the core axis remains fixed (impulse approximation). It is thus best described in the molecular frame. Due to the cylindrical symmetry of this potential the projection  $\Lambda = \mathbf{L} \cdot \hat{\mathbf{M}}$  of  $\mathbf{L}$  onto the core axis  $\hat{\mathbf{M}}$  is conserved. With

the auxiliary approximation that  $L^2$  is constant, this amounts to the collision being described by a precession of  $\mathbf{L}$  around  $\hat{\mathbf{M}}$  by an angle  $\delta\varphi_L$ . Furthermore the invariance of the potential under reflection with respect to any plane containing  $\hat{\mathbf{M}}$  implies that  $\delta\varphi_L$  is odd with respect to  $\theta_L \rightarrow \pi - \theta_L$ . The simplest choice is  $\delta\varphi_L = K \cos \theta_L$ , which defines the strength  $K$  of the interaction. Notice that this  $\theta_L$  dependant rotation about the  $OZ$  molecular axis is a twist, not a global rotation of the sphere, implying that the dynamics generated by the map can be chaotic [27,28]. Since  $\mathbf{L}$  has changed, at least in direction if we make the approximation  $L^2$  constant, due to the conservation of total angular momentum  $\mathbf{J} = \mathbf{L} + \mathbf{N}$ ,  $\mathbf{N}$  changes both in direction and in magnitude. This has far reaching consequences. The change of the magnitude entails a change of the rotational energy of the core  $E_N = BN^2$  ( $2B$  is the reciprocal of the core moment of inertia  $I$  according to usual spectroscopic notation [29]). Consequently, due to the conservation of the total energy  $E$  the electron's energy  $E_e = E - E_N$  also changes. If  $E_e$  becomes positive the molecule ionizes, if it remains negative the resulting changes of  $T_e$  and  $T_N$  will change the parameters of the next Coulomb step. While the “quantum” molecular reference frame is fixed during the collision, in the “classical” molecular reference frame, its  $OX_C$  axis, which is chosen along  $\mathbf{N}$ , will change (Fig. 2(c)). This produces an additional phaseshift  $\delta\varphi'_L$ , which was called frame recoil in ref. [8] where explicit formulae are given. It can also be computed from eq. (A.3) of Appendix A.1, which gives the angular position of  $\mathbf{N}$  in the fixed “quantum” molecular frame, by taking the difference of positions before and after the  $\delta\varphi_L$  kick.

- (ii) Coulomb (or free rotation) step: when  $r \gg r_0$  the electron only feels the spherically symmetric  $-1/r$  part of the potential. It moves on a Kepler orbit. Its angular momentum  $\mathbf{L}$  and its Laplace-Runge-Lenz vector  $\mathbf{A}$  are constant in the laboratory  $Oxyz$  reference frame. Meanwhile the molecular core rotates at constant speed around its angular momentum  $\mathbf{N}$  which is perpendicular to its axis  $\hat{\mathbf{M}}$ . When seen in the “classical” molecular frame, with  $OZ$  along  $\hat{\mathbf{M}}$  and  $OX_C$  along  $\mathbf{N}$  (Fig. 2(c)),  $\mathbf{L}$  (and  $\mathbf{A}$ ) seem to rotate the opposite way (clockwise) around  $OX_C$ . The total angle of rotation is  $\delta\beta = -2\pi T_e/T_N$ , *i.e.* the ratio of the periods of the electron orbit and of the core rotation. We have  $T_e = 2\pi(-2E_e)^{3/2}$  a.u. and  $T_N = 2\pi/2BN$  a.u..

The crucial point of this model is the exchange of energy between the electron and the core during the collision step. If we neglected it the model would coincide with with a “kicked spin” model [30,31], which cannot lead to ionization.

For the free rotation step we prefer to visualize the results in the “classical” molecular frame. Indeed in the “quantum” molecular frame the free rotation is about a direction of  $\mathbf{N}$  in the molecular  $OX_QY_Q$  plane (see Fig. 2(b)), which varies from step to step. We will visualize ionization on the Poincaré sphere in

the “classical” frame by noting that positive electron energies  $E_e$  correspond to points where the total energy  $E$  is greater than the rotational energy  $E_N$ . Using  $\mathbf{J}^2 = (\mathbf{L} + \mathbf{N})^2$ , this leads to the inequality

$$E_N = BN^2 = B \left( -L \cos \alpha + \sqrt{J^2 - L^2 \sin^2 \alpha} \right)^2 < E \quad (1)$$

This condition only depends on the angle  $\alpha$  between  $\mathbf{L}$  and  $\mathbf{N}$  and accordingly the positive electron energy region corresponds to a cap around the positive  $\mathbf{N}$  axis, which is fixed in this frame (Fig. 2(c)). If we relax the condition  $L^2$  constant, we have a four dimensional PM and formulae for the collision and the recoil are modified, but eq. (1) remains valid.

Practically, there are two possibilities to compute the classical PM. In all our previous works, we considered it entirely in the “classical” molecular reference frame, by computing in turn free rotation, collision  $\delta\varphi_L$ , frame recoil, new values of  $N$ ,  $E_N$ ,  $T_N$ ,  $E_e$ ,  $T_e$  and plotting the results in the “classical” reference frame by using equations given in Appendix A.1. In the present work we alternate between laboratory frame and “quantum” reference frame, in a way summarized in the first three columns of table 1 (the last two will be filled below in sections 3 and 5). We choose this more complex, and thus slower, procedure, because as outlined in section 5, the coordinates in the “classical” reference frame are not canonically conjugate. This is of no harm for purely classical computations, but forbids the semi-classical analysis. Of course we have checked that both representations give the same results.

Finally we will describe how to construct the combined Poincaré–Jung scattering map. The JSM is defined such that the electron which escapes to infinity is fed back by doing a step backwards in time without collision with the core (i.e. a pure Coulomb step with reverted velocity), and then re launching the electron towards the molecule along the resulting asymptotic trajectory for the next collision (Fig. 1(b)). Notice that  $\mathbf{L}$  and  $\mathbf{A}$  are constant in the *laboratory* frame during such a pure Coulomb step. For the  $L^2$  constant case this amounts to starting from the same point on the Poincaré sphere in the *molecular* frame if  $E_e > 0$  after a collision, i.e. to skip the three first steps in Table 1. Indeed the rotation of the core is neglected during the impulse collision step, and during journeys to and from infinity of the electron these rotations cancel since they are made for  $r > r_0$ , where the short range potential is negligible. In the general case the “argument of the perihelion”  $\omega$  is also conserved. The proper JSM is a map from ionized to ionized states, the PM a map from bound to bound states, but there is obviously no technical problem to iterate a combined map from unbound to bound states and vice versa by selecting the JSM recipe to feed back ionizing trajectories. This seemingly strange feed back was suggested and discussed in ref. [14]. We shall show that it is indeed a good representation of the results in quantum mechanics under semi-classical conditions.

Table 1

Poincaré Map: summary. Molecular coordinates are in the “quantum” reference frame.

Coords.	Action	Classical	MQDT	Semi Classical
$L'_Z \varphi'_L$	M.→L.	eqs.(A.8,A.11)	$\hat{U}_{N'\Lambda'}^{(LJ)}$	$F_3(L'_Z, \varphi_{N'})$ eq.(42)
$N' \varphi_{N'}$	Free r.	$\delta\varphi_N = \begin{cases} 2\pi \frac{T'_e}{T'_N} \\ -2\pi \frac{\partial \nu_{N'}}{\partial N'} \end{cases}$	$e^{2i\pi\nu_{N'}}$	$F_3(N', \varphi_N) = N' \varphi_N + 2\pi\nu_{N'}$
$N' \varphi_N$	L.→M.	eqs.(A.14,A.15)	$\hat{U}_{\Lambda N'}^{\dagger(LJ)}$	$F_2(\varphi_N, L_Z)$ eq.(42)
$L_Z \varphi''_L$	Coll.	$\delta\varphi_L = \begin{cases} 2K \cos \theta_L \\ -2\pi \frac{\partial \mu_\Lambda}{\partial \Lambda} \end{cases}$	$e^{2i\pi\mu_\Lambda}$	$F_3(L_Z, \varphi_L) = L_Z \varphi_L + 2\pi\mu_{L_Z}$
$L_Z \varphi_L$				

### 3 MQDT as a generalized quantum Poincaré map

#### 3.1 The usual MQDT theory

MQDT for molecules is a well established, time honored theory [2,3,4,5]. We will outline here only what is needed for our purposes. The theory closely parallels the preceding classical ideas, which originated from the classical limit of MQDT, but which were implicitly present in Fano’s seminal paper [2], albeit with a fully quantum way of writing down the theory. Wave functions have different forms for  $r \lesssim r_0$  and  $r \gtrsim r_0$  and they are matched at  $r = r_0$ . Going from  $r = 0$  to  $r = \infty$  we have

- (i) Collision step:  $r \lesssim r_0$ . The electron’s motion is rigidly coupled to the molecular axis  $\hat{\mathbf{M}}$ . Its speed exceeds by far the speed of the motions of the nuclei of the molecular ion and the Born-Oppenheimer factorization of the molecular wave function applies (Hund’s case (b) coupling type according to molecular spectroscopy nomenclature[29]). Due to the cylindrical symmetry of the potential the projection  $\Lambda = \mathbf{L} \cdot \hat{\mathbf{M}}$  of the electron’s angular momentum onto the molecular axis  $\hat{\mathbf{M}}$  is a constant of the motion, whereas the squared angular momentum  $\mathbf{N}^2$  of the molecular ion rotation does not have a definite value. We may or may not have a definite value of  $L^2$  depending on the use of the auxiliary approximation

$L^2 = \text{const.}$  The angular part of the wave function is thus an eigenfunction of  $\Lambda$  (in addition to  $J$  and  $M_J$ ) denoted by  $X_{M_J}^{(J,\Lambda)}(\theta'_e, \varphi'_e, \hat{\mathbf{M}})$  [2], where  $(\theta'_e, \varphi'_e)$  are the angular coordinates of the Rydberg electron in the “quantum” *molecular* reference frame  $OX_QY_QZ_Q$  defined in Fig. 2(b) and Appendix A. For  $r \sim r_0$ , i.e. outside of the molecular core, where the potential is approximately pure Coulomb, the radial part of the Rydberg electron wave function is a linear combination of two independent Coulomb functions. We choose the one regular at  $r = 0$ ,  $s(E_e, r)$ , as well as one irregular at  $r = 0$ ,  $c(E_e, r)$ , suitably selected for its asymptotic properties when  $r \rightarrow \infty$  [1]. The normalized total wave function reads [2] as

$$\Psi_\Lambda(\theta'_e, \varphi'_e, \hat{\mathbf{M}}; r) = X_{M_J}^{(L,J,\Lambda)}(\theta'_e, \varphi'_e, \hat{\mathbf{M}}) (s(E_e, r) \cos(\pi\mu_\Lambda) + c(E_e, r) \sin(\pi\mu_\Lambda)). \quad (2)$$

This implicitly defines the “quantum defects”  $\mu_\Lambda$ . Notice that  $E_e$  depends on  $\Lambda$ . If the subsidiary approximation  $L^2$  constant is not used, the  $X$ 's are not eigenstates of  $L^2$ , but can be developed in such a basis, implying a summation over  $L$  and an extra label  $L$  on the  $\mu$ 's and the  $E_e$ 's. The quantum defects can in principle be computed by ab initio electronic molecular calculations between  $r = 0$  and  $r = r_0$ , but we will take them here as semi empirical parameters, as is frequently done. We will assume that they are independent of energy, in a restricted range above or below zero electron energy. This is justified by the fact that in the inner region the change of the total energy is negligible as compared to the electron kinetic energy in the Coulomb well. The wave function in the collision region should not depend significantly on such small variations of the total energy. For large distances there is a difference, leading to bound or unbound states. We will neglect refinements used in actual molecular calculations to compute levels with somewhat lower principal quantum numbers, for which one allows quantum defects to vary slowly with  $E_e$ .

- (ii) Coulomb step:  $r \gtrsim r_0$ . The electron is coupled to the isotropic part of the Coulomb potential only, and cannot exchange angular momentum with the core. The core angular momentum  $N$  and the electron angular momentum  $L$  are thus separately conserved, as is  $\mathbf{J} = \mathbf{L} + \mathbf{N}$ . The angular part of the wave function  $\Phi_{M_J}^{(L,J,N)}(\theta_e, \varphi_e, \hat{\mathbf{M}})$  corresponds to the coupling by a Clebsch-Gordan coefficient of an electron wave function labeled by  $L$  and of a molecular core wave function labeled by  $N$  (Hund's case (d) coupling type according to molecular spectroscopy nomenclature[29]). Here  $(\theta_e, \varphi_e)$  are the electron coordinates in the *laboratory* reference frame  $Oxyz$ . The radial part of the wave function of the Rydberg electron is again a linear combination of regular and irregular Coulomb wave functions. The total wave function reads

$$\Psi_N(\theta_e, \varphi_e, \hat{\mathbf{M}}; r) = \Phi_{M_J}^{(L,J,N)}(\theta_e, \varphi_e, \hat{\mathbf{M}}) (s(E_e, r) c_N + c(E_e, r) d_N), \quad (3)$$

where  $E_e = E - BN(N+1)$  can be positive or negative and  $c_N$  and  $d_N$  are to be determined from asymptotic conditions. Here again an additional summation over  $L$  is necessary when omitting the auxiliary approximation that  $L^2$  be conserved.

For  $r \sim r_0$  we have one and the same wave function developed into two different bases (2) and (3). The electron angular parts correspond to a change from the molecular frame to the laboratory frame. The orthogonal matrix  $\hat{U}$  which performs this change [2],

$$X_{M_J}^{(L,J,\Lambda)} = \sum_N \Phi_{M_J}^{(L,J,N)} \hat{U}_{N\Lambda}^{(LJ)}, \quad (4)$$

is proportional to a Clebsch-Gordan coefficient:

$$\hat{U}_{N\Lambda}^{(LJ)} = \langle L - \Lambda J \Lambda | L J N 0 \rangle (-1)^{J-N+\Lambda} (2 - \delta_{\Lambda 0})^{\frac{1}{2}}, \quad (5)$$

if we use the definition of rotational wave functions given in Appendix A.

We transform a general wave function  $\Psi = \sum_{\Lambda} \Psi_{\Lambda} A_{\Lambda}$  from the molecular to the laboratory frame by combining (2) and (4). The matching of the wave functions (2) and (3) yields

$$\begin{aligned} \Psi(\theta_e, \varphi_e, \hat{\mathbf{M}}; r) &= \sum_N \Phi_{M_J}^{(L,J,N)}(\theta_e, \varphi_e, \hat{\mathbf{M}}) \Psi_N(r) \\ \Psi_N(r) &= \sum_{\Lambda} \hat{U}_{N\Lambda} (s(E_e, r) \cos(\pi\mu_{\Lambda}) + c(E_e, r) \sin(\pi\mu_{\Lambda})) A_{\Lambda} \end{aligned} \quad (6)$$

taking into account that the implicit  $E_e$  dependance of the radial wave functions on  $\Lambda$  in eq. (2) and on  $N$  in eq. (3) is negligible *near*  $r \sim r_0$ . This would be true neither for  $r \ll r_0$  nor for  $r \gg r_0$ .

The coefficients  $A_{\Lambda}$  in eq. (6) are obtained from the asymptotic properties of the wave function for  $r \rightarrow \infty$ . These properties in turn depend on whether the electronic energy in each asymptotic channel labeled by  $N$ , namely  $E_e = E - BN(N+1)$ , is positive (open channels) or negative (closed channels). In any case we define a principal quantum number  $\nu_N$  (non integer) by  $E_e = -1/2\nu_N^2$ . For closed channels  $\nu_N$  is real, for open channels it is imaginary.

In a *closed* channel, for the motion to be bounded, the exponentially increasing part of the Coulomb wave function must be zero, which implies that the radial part  $\Psi_N(r)$  of the wave function in eq. (6) must be proportional to a suitable combination of regular and irregular Coulomb wave functions which is regular when  $r \rightarrow \infty$ , i.e. of the form: [1,32]:

$$\Psi_N(r) \propto -\cos(\pi\nu_N) s(E_e, r) + \sin(\pi\nu_N) c(E_e, r), \quad (7)$$

Combining equations (6) and (7) yields

$$\sum_{\Lambda} \hat{U}_{N\Lambda} \sin(\pi(\nu_N + \mu_{\Lambda})) A_{\Lambda} = 0 \quad (8)$$

In an *open* channel the Coulomb wave function may be decomposed into incoming and outgoing Coulomb waves  $\varphi^{\pm}$  which have the asymptotic behavior [1]:

$$\begin{aligned} \varphi^{\pm}(r) &= \frac{1}{\sqrt{2}} (c \pm is) \sim (\pi k)^{-\frac{1}{2}} \exp(\pm i\zeta) && \text{for } r \rightarrow \infty \quad (9) \\ \zeta &= kr - \frac{1}{2}L\pi + \frac{1}{k} \ln(2kr) + \arg(\Gamma(L + 1 - ik)), && k = \frac{i}{\nu_N}. \end{aligned}$$

Scattering is defined with respect to pure Coulomb scattering, that is, the eigenphases  $\tau$  are measured relative to the Coulomb phases  $\zeta$ . The wave function will have the correct asymptotic behavior in the limit  $r \rightarrow \infty$  for the asymptotic channel  $N$  if its radial part is of the form:

$$\Psi_N(r) \propto \sum_{N'} C_{N'} \left( \varphi^-(\nu_N; r) \delta_{NN'} - \varphi^+(\nu_N; r) \hat{S}_{NN'} \right), \quad (10)$$

where the sum runs *only* over all *open* channels, and the  $C_{N'}$  are constants to be related to the  $A_{\Lambda}$ . This defines the scattering matrix  $\hat{S}$ . It is interesting to consider the matrix  $\hat{T}$  which diagonalizes  $\hat{S}$ , i.e.

$$\hat{S}_{NN'} = \sum_{\ell} \hat{T}_{N\ell} \exp(2i\pi\tau_{\ell}) \hat{T}_{\ell N'}^t \quad (11)$$

Using eq. (9), we obtain:

$$\begin{aligned} \Psi_N(r) &\propto \sum_{\ell} \Psi_{N\ell}(r) \\ \Psi_{N\ell}(r) &= \left( \frac{\sqrt{2}}{i} \sum_{N'} C_{N'} \hat{T}_{\ell N'}^t \exp(-i\pi\tau_{\ell}) \right) \times \\ &\quad \hat{T}_{N\ell}(s(E_e, r) \cos(\pi\tau_{\ell}) + c(E_e, r) \sin(\pi\tau_{\ell})) \end{aligned} \quad (12)$$

Near  $r \sim r_0$  eq. (6) should have this form and we obtain, for each value of  $\ell$ , two equations:

$$0 = \sum_{\Lambda} \hat{U}_{N\Lambda} \sin(\pi(\mu_{\Lambda} - \tau_{\ell})) A_{\Lambda}(\ell) \quad (13)$$

$$\hat{T}_{N\ell} \propto \sum_{\Lambda} \hat{U}_{N\Lambda} \cos(\pi(\mu_{\Lambda} - \tau_{\ell})) A_{\Lambda}(\ell) \quad (14)$$

Equations (8) and (13) can be combined to

$$\hat{\mathcal{S}}|A(\ell)\rangle = 0 \quad (15)$$

with

$$\hat{\mathcal{S}} = \begin{pmatrix} \hat{U}_{N\Lambda} \sin(\pi(\mu_\Lambda - \tau_\ell)) & ; N \text{ open} \\ \hat{U}_{N\Lambda} \sin(\pi(\mu_\Lambda + \nu_N)) & ; N \text{ closed} \end{pmatrix} \quad (16)$$

where  $\mathcal{S}$  stands for sine, not to be confused with the  $S$  matrix in eq. (11).

### 3.2 MQDT as a Quantum Poincaré map

We now seek an alternative along the lines sketched in ref. [13] for the case of all channels closed. The matrix  $\hat{\mathcal{S}}$  defined in eq. (16) is the imaginary part of a *complex unitary* matrix

$$\hat{\mathcal{E}} = \hat{\mathcal{C}} + i\hat{\mathcal{S}} = \begin{pmatrix} \hat{U}_{N\Lambda} \exp(i\pi(\mu_\Lambda - \tau_\ell)) & ; N \text{ open} \\ \hat{U}_{N\Lambda} \exp(i\pi(\mu_\Lambda + \nu_N)) & ; N \text{ closed} \end{pmatrix} \quad (17)$$

Splitting real and imaginary parts in the unitarity relation

$$\hat{\mathcal{E}}^\dagger \hat{\mathcal{E}} = (\hat{\mathcal{C}}^t - i\hat{\mathcal{S}}^t)(\hat{\mathcal{C}} + i\hat{\mathcal{S}}) = \hat{\mathbb{I}} \quad (18)$$

gives

$$\hat{\mathcal{C}}^t \hat{\mathcal{C}} + \hat{\mathcal{S}}^t \hat{\mathcal{S}} = \hat{\mathbb{I}} \quad (19)$$

$$\hat{\mathcal{C}}^t \hat{\mathcal{S}} = \hat{\mathcal{S}}^t \hat{\mathcal{C}} \quad (20)$$

Equation (20) implies that if  $|A(\ell)\rangle$  is an eigenvector of  $\hat{\mathcal{S}}$  with eigenvalue zero, then  $|B(\ell)\rangle = \hat{\mathcal{C}}|A(\ell)\rangle$  is an eigenvector of  $\hat{\mathcal{S}}^t$  with eigenvalue zero, i.e. a solution of the transpose of eq. (15):

$$\hat{\mathcal{S}}^t |B(\ell)\rangle = 0 \quad (21)$$

Writing down the components of  $|B(\ell)\rangle$ ,

$$B_N(\ell) = \sum_{\Lambda} \hat{\mathcal{C}}_{N\Lambda} A_\Lambda(\ell) \quad (22)$$

we see that the matrix  $\hat{\mathcal{C}}$  relates the eigenfunction for channel  $\ell$  in the molecular reference frame labeled by  $\Lambda$  to that in the laboratory reference frame labeled by  $N$ . Note that eq. (22) is the same as eq. (14), except that the matrix  $\hat{T}$  is defined for *open* channels only, while  $B$  is defined for *all* channels.

Next, consider the *symmetric complex unitary* matrix:

$$\begin{aligned}\hat{\mathcal{E}}^t \hat{\mathcal{E}} &= (\hat{\mathcal{C}}^t + i \hat{\mathcal{S}}^t)(\hat{\mathcal{C}} + i \hat{\mathcal{S}}) \\ &= (\hat{\mathbb{I}} - 2 \hat{\mathcal{S}}^t \hat{\mathcal{S}}) + 2i \hat{\mathcal{C}}^t \hat{\mathcal{S}},\end{aligned}\tag{23}$$

using eqs. (19,20). This implies that if  $\hat{\mathcal{S}}|A_\Lambda\rangle = 0$ , then

$$\hat{\mathcal{E}}^t \hat{\mathcal{E}}|A_\Lambda\rangle = \hat{\mathbb{I}}|A_\Lambda\rangle,\tag{24}$$

i.e. the solutions of eq. (15) are eigenvectors of  $\hat{\mathcal{E}}^t \hat{\mathcal{E}}$  with eigenvalue 1.

Similarly the  $|B_N\rangle$  are eigenvectors of  $\hat{\mathcal{E}} \hat{\mathcal{E}}^t$  with eigenvalue 1

$$\hat{\mathcal{E}} \hat{\mathcal{E}}^t |B_N\rangle = \hat{\mathbb{I}}|B_N\rangle\tag{25}$$

Eqs. (24,25) imply the determinant equation

$$\det(1 - \hat{\mathcal{E}}^t \hat{\mathcal{E}}) = 0.\tag{26}$$

Comparing this result with the equation for the  $T(E_n)$  matrix defined by Bogomolny [9,10,11] was essential for the interpretation of MQDT as a QPM in ref. [13]. We will examine this relation more closely in the next sections.

For scattering systems we have to go a little further, because we have to search for the phase shifts at any energy rather than for eigenvalues and eigenfunctions. For this situation we shall derive another useful form of these equations. Remember that in this case vectors and matrices in eqs. (24,25) depend on the channel number  $\ell$  and that the  $B_N(\ell)$  are identical to the eigenvectors  $T_{N\ell}$  of the  $S$  matrix. We are looking for a set of equations written for open channels only, whereas eq. (24) is written for all channels, open and closed. For this purpose we write eq. (25) in bloc diagonal form, splitting the  $N$  channels into open channels indexed by  $o$  and closed channels indexed by  $c$ . This is possible for elements indexed by the asymptotic quantum number  $N$ , e.g.  $\hat{\mathcal{E}} \hat{\mathcal{E}}^t$ , not for those indexed by the Born Oppenheimer quantum number  $\Lambda$ , e.g.  $\hat{\mathcal{E}}^t \hat{\mathcal{E}}$ . We obtain

$$(\hat{\mathcal{E}} \hat{\mathcal{E}}^t)_{oo} B_o + (\hat{\mathcal{E}} \hat{\mathcal{E}}^t)_{oc} B_c = B_o\tag{27}$$

$$(\hat{\mathcal{E}} \hat{\mathcal{E}}^t)_{co} B_o + (\hat{\mathcal{E}} \hat{\mathcal{E}}^t)_{cc} B_c = B_c\tag{28}$$

Eliminating  $B_c$  gives

$$\left( (\hat{\mathcal{E}} \hat{\mathcal{E}}^t)_{oo} + (\hat{\mathcal{E}} \hat{\mathcal{E}}^t)_{oc} \left( \hat{\mathbb{I}}_{cc} - (\hat{\mathcal{E}} \hat{\mathcal{E}}^t)_{cc} \right)^{-1} (\hat{\mathcal{E}} \hat{\mathcal{E}}^t)_{co} \right) B_o = B_o\tag{29}$$

Notice then that we can rewrite eq. (17) as

$$\hat{\mathcal{E}} = \exp(i\pi\hat{\nu}) \hat{U} \exp(i\pi\hat{\mu}) \quad (30)$$

where  $\hat{\nu}$  is the diagonal matrix in the laboratory reference frame with diagonal elements

$$\hat{\nu}_{NN} = \begin{cases} -\tau_\ell & ; N \text{ open} \\ +\nu_N & ; N \text{ closed} \end{cases} \quad (31)$$

and  $\hat{\mu}$  is the diagonal matrix in the molecular reference frame with diagonal elements  $\mu_\Lambda$ .

Then, defining

$$\hat{\mathcal{U}} = \hat{U} \exp(2i\pi\hat{\mu}) \hat{U}^t \quad (32)$$

Equation (29) can be rewritten as

$$\left( \hat{\mathcal{U}}_{oo} + \hat{\mathcal{U}}_{oc} \left( \exp(-2i\pi\hat{\nu})_{cc} - \hat{\mathcal{U}}_{cc} \right)^{-1} \hat{\mathcal{U}}_{co} \right) B_o(\ell) = \exp(2i\pi\tau_\ell) B_o(\ell) \quad (33)$$

The matrix within the left large parenthesis no longer depends on  $\tau_\ell$ ; it is defined in open channels, and for each  $\ell$  has the same eigenvalue (eq. (11)) and the same eigenvector (eqs. (14) and (22)) as the  $S$  matrix. We thus obtain the expression

$$\hat{S} = \hat{\mathcal{U}}_{oo} + \hat{\mathcal{U}}_{oc} \left( \exp(-2i\pi\hat{\nu})_{cc} - \hat{\mathcal{U}}_{cc} \right)^{-1} \hat{\mathcal{U}}_{co} \quad (34)$$

for the  $S$  matrix.

### 3.3 Computational advantages

The usual MQDT (sec. 3.1) uses the equation  $\det \hat{S} = 0$  (eq. 16) which can be rewritten as a polynomial in  $\tan(\pi\tau_\ell)$  whose degree equals the number of open channels. Each root gives a well defined  $\tau$  because, according to eq. (11), the eigenphases of the  $\hat{S}$  matrix can take values between 0 and 1 (or -0.5 and 0.5) only. Depending on the choice of the total energy there are the possibilities that all channels are closed (there is then only one value of the set  $\{A_\Lambda\}$ ) or open. In the last case one obtains as obvious solutions the values  $\tau_\ell = \mu_\Lambda$  (see (eq. 16)). This shows that the  $\mu_\Lambda$  are exactly the usual collision phase shifts when the energy is high enough for all channels to be open. In the general case equation (16) is not solved by a diagonalization algorithm. The usual way to find a solution is

- All channels closed: No  $\tau_\ell$ . All matrix elements depend on energy  $E$  through the  $\nu_N$ . One varies  $E$  and locates the zeros of the determinant by a root searching algorithm.

- Some channels closed, some open. One fixes a given value of  $E$  and searches the values of  $\tau_\ell$  for which the determinant vanishes. The search may be done by computing the determinant and varying  $\tau_\ell$  like in the preceding case, or by writing the polynomial in  $\tan \tau_\ell$  and computing its roots. In any case it is a root searching algorithm.

As explained in ref. [13], where illuminating figures are given, the practical problem with such a standard approach is that when zeros are very close the determinant crosses twice or more often the zero line at extremely close values, and nearly tangent to the zero line. This makes it very difficult to avoid the missing of some pairs of zeroes. Moreover, in such a situation it is very difficult to recover the wavefunctions individually as they switch between nearly orthogonal states for a very small change of  $E$  or  $\tau_\ell$ . This situation is quite common in the case of a nearly integrable phase space, where there are systematic near degeneracies associated to the lack of level repulsion due to approximately conserved quantum numbers. The problem of missing levels becomes particularly severe for the high values of angular momenta we use to study the semi classical limit.

In our QPM formulation (sec. 3.2) for bound systems the relevant practical aspect [13] was that we could diagonalize the unitary matrix  $\hat{\mathcal{E}}^t \hat{\mathcal{E}}$  by standard techniques. Then the equation is solved by a search of zeros of the eigenphases, which move monotonously as a function of energy. Though it still requires a root searching algorithm, it is much more efficient for near degenerate levels than the standard MQDT equation  $\det \hat{\mathcal{S}} = 0$  and may be accelerated by linear interpolation. In the case of approximate double degeneracies, the diagonalization algorithm always reliably provides a good pair of orthogonal wavefunctions.

Similarly in the ionized case the computation of the  $S$  matrix with eqs. (33,34) is reduced to a standard diagonalization of a *complex symmetric* matrix (for any *real energy*), with an auxiliary inversion of a matrix in the closed channel space. The components of the resulting wave function on the open channels ( $B_o(\ell) \equiv T_{o\ell}$ ) are obtained by the diagonalization and the components on the closed channels are then deduced with eq. (28). An other way to use this equation is to look for the zeros of the matrix to invert in the *complex energy* plane, which gives poles of the  $\hat{\mathcal{S}}$  matrix. We will use both techniques in the next sections.

## 4 Comparison between classical and quantum evolution on the surface of section

### 4.1 Principles

One of the basic tools we use to study properties of our molecular system is to compare the PM with Husimi [33] or Wigner [34] plots of eigenfunctions, as well as the time evolution of such quantum distributions in phase space with that of a swarm of classical trajectories. In such plots we represent the angular part of the wave function, ignoring its radial part. In other words we represent both the classical and the quantum evolution on the surface of section, thus relating the PM and the QPM.

First we recall that we can perform the comparison of such objects in two different frames, the molecular or Born-Oppenheimer frame and the laboratory frame. The molecular frame wave functions have coefficients labeled by  $\Lambda$ , the laboratory frame wave functions have coefficients labeled by  $N$ . The coefficients of a given wave function in those two reference frames are related by eq. (22). According to eq. (17) the matrix  $\hat{\mathcal{C}}$  which performs the transformation is composed of the matrix  $\hat{U}$ , which transforms between the molecular and the laboratory frames and of phase shifts in the two frames. We will explain the meaning of these phase shifts at the end of this section. Note that, according to [35, eq. (A2.1)], the asymptotic value of  $\hat{U}$  for large angular momenta reduces to a rotation of  $\pi/2$  around  $OY$ .  $\hat{U}$  thus basically performs a rotation between two orthogonal polar axis  $\hat{\mathbf{M}}$  and  $\mathbf{N}$ . We shall focus on four key points in an electron orbit: perigee, apogee, and the two crossings of the surface of the sphere of radius  $r_0$ , the border between the free motion and the collision region. For hyperbolic motion the apogee does not exist. Wave functions for all these four points are naturally contained in the MQDT. Perigee coefficients are the  $A_\Lambda$  introduced in eq. (6). They are naturally expressed in the laboratory frame. In the case where all channels are bound, apogee coefficients are the components  $B_N$  of the eigenvector  $|B\rangle$  of  $\hat{\mathcal{S}}^t$  introduced in eqs. (21,22). They are naturally expressed in the laboratory frame, but may be expressed in the molecular frame by multiplication with the matrix  $\hat{U}^t$ . The coefficients at the crossing of the sphere of radius  $r_0$  before and after collision are the angular parts of incoming  $\varphi^-(r)$  and outgoing  $\varphi^+(r)$  in eq. (10). They are defined for unbound motion, but the basis for the validity of MQDT is that at  $r_0$  the inner part of the wave function is approximately the same for bound and unbound motion. So even for bound motion one can speak of “infinitely far from the core” motion at  $r_0$ . This was a key point for the derivation of the classical limit of MQDT in ref. [8]. The incoming and outgoing angular parts are naturally defined in the laboratory frame, but inserting eq. (9) into eq. (6) we see that they are respectively  $e^{i\pi\hat{\mu}} A_\Lambda$  and  $e^{-i\pi\hat{\mu}} A_\Lambda$  in the molecular frame.

These considerations are clearly displayed by combining eqs. (24) and (30):

$$\begin{aligned} 0 &= \det(\hat{\mathbb{I}} - \hat{\mathcal{E}}^t \hat{\mathcal{E}}) \\ &= \det(\hat{\mathbb{I}} - e^{i\pi\hat{\mu}} \hat{U}^t e^{i\pi\hat{\nu}} e^{i\pi\hat{\nu}} \hat{U} e^{i\pi\hat{\mu}}), \end{aligned} \quad (35)$$

As written this is the determinant of a matrix in the molecular frame. It represents a QPM between perigee and perigee, and the associated eigenfunctions are the  $|A_\Lambda\rangle$ . These are the angular part of the perigee wave function. They depend on the energy  $E$  and (if there are open channels) on the phase shift  $\tau_\ell$  which cause the determinant to vanish. The second line of this equation reads, from right to left: apply half a collision ( $e^{i\pi\hat{\mu}}$ ), rotate the axis from  $OZ$  to  $OX$  by  $\hat{U}$ , apply half a free rotation ( $e^{i\pi\hat{\nu}}$ ), you are at the apogee. Then apply half a free rotation, rotate from  $OX$  to  $OZ$ , apply half a collision and you are back to the perigee.

One may cyclically interchange the matrices in the product entering the determinant. Then eigenfunctions of the associated matrix are transformed accordingly. Moving the matrices step by step one place from left to right this gives first the QPM for the outgoing wave,  $|e^{i\pi\hat{\mu}\Lambda} A_\Lambda\rangle$  in the molecular frame, then the same QPM in the laboratory frame, next the QPM between apogee and apogee in the laboratory frame *etc.* This provides the explanation for the phase shifts included in eq. (22): going from  $A_\Lambda$  to  $B_N$  involves not only a change of the basis, but also half a collision, and half a free rotation.

#### 4.2 All channels closed

That this is the correct interpretation is illustrated in Fig. 3, where we compare the time evolution of a (quantum mechanical) Husimi distribution and a corresponding classical swarm of trajectories for a bound system. The parameters correspond to a mean energy for which  $T_e/T_N = 1/3$ , so that a free rotation is 1/3 of a turn, and a strong coupling  $K = -3.98765\pi$  giving a strong stretch around  $OZ$ , nearly  $\pm$  two full turns at the  $\pm OZ$  poles (and zero at the equator). The remaining parameters are chosen as  $L = 40$ ,  $J = 200$ ,  $2B = 2.5 \cdot 10^{-12}$  a.u.. The angular momenta are large as compared to those accessible in current molecular experiments, especially  $L$  which usually is limited to the range 0-2 in two step laser excitations. They correspond to semi classical scaling of the experimental situation [6,7], as explained in section 2.3.

The quantum time evolution is computed by first obtaining a set of  $2L + 1$  consecutive eigenenergies  $E_i$  and the corresponding angular wave functions  $A_\Lambda^i$  for increasing principal quantum number  $\nu_J$  by one (or a multiple of such sets to increase statistical accuracy of the results). An initial radial wave function

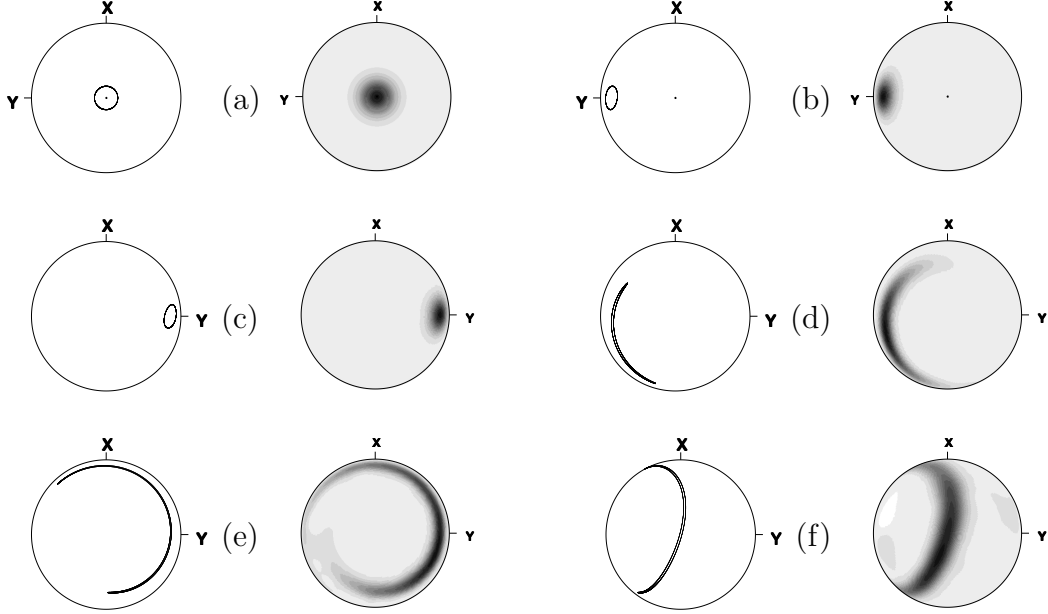


Fig. 3. Comparison between Classical and Quantal time evolution. All channels closed. Parameters  $\nu_J = 875 - 880$  a.u.,  $\mu_{40} = 39.8765$ , corresponding to  $T_e/T_N = 1/3$ ,  $K = -3.98765\pi$ . (a): Start. (b)-(d): Application of  $\hat{\mathcal{E}}$ . Half a free rotation ( $e^{i\pi\hat{\nu}}$ ),  $1/6$  of a turn clockwise around  $OX$  leads from (b) to (c) (notice the flip from top view to bottom view),  $U$  changes axis from  $OX$  to  $OZ$ , half a collision ( $e^{i\pi\hat{\mu}}$ ), stretch around  $OZ$  leads from (c) to (d). (d)-(f): Application of  $\hat{\mathcal{E}}^t$ . Half a stretch around  $OZ$ ,  $\hat{U}^t$ , half a rotation around  $OX$ .

is then expanded in this eigenbasis. The time evolution results by applying  $\exp(iE_i t)$  to the  $A_\Lambda^i$ . Notice that it is applied only to the angular part, not to the radial part of the wave functions. But for integer times, which correspond to a full orbit because we express energies in terms of a mean  $\nu$ , the radial part is the same, so the corresponding radial overlap is one. This procedure is consistent with the QPM point of view. What we neglect in doing so, is the spreading with time of the radial wave packet. This is consistent with a semi classical picture. For a full quantum computation we would need to choose a radial distribution  $f(r)$  peaked around the corresponding radius  $r$ , perigee, apogee,  $r_0$ , and to develop this initial state, angular and radial part, in an eigenbasis. The initial quantum distribution is the Husimi distribution of a  $|LL\rangle$  state. The corresponding classical distribution is a circle around  $OZ$  with radius given by  $\cos\theta_L = L/\sqrt{L(L+1)}$ . In Fig. 3 the top pair (a) equally corresponds to incoming, perigee and outgoing waves because the collision is a rotation around  $OZ$  and the distribution is rotationally invariant around this axis. The next pair (b) is the apogee. Quantum mechanically we cannot compute it from the previous distribution because we can compute only the evolution with an integral number of turns. It is thus obtained by a rotation of the initial distribution around  $OX$  by  $1/6$  of a turn. But then everything is computed from the four initial distributions by applying the above method.

One sees perfectly the evolution: 1/6 of a turn around  $OX$  (c), half stretch around  $OZ$  (d), half stretch along  $OZ$  (e), 1/6 of a turn around  $OX$  (f) etc. The quantum distribution follows perfectly the classical one in such short times. For longer times they begin to differ due to the finite value of  $\hbar$ .

### 4.3 First Channel Open

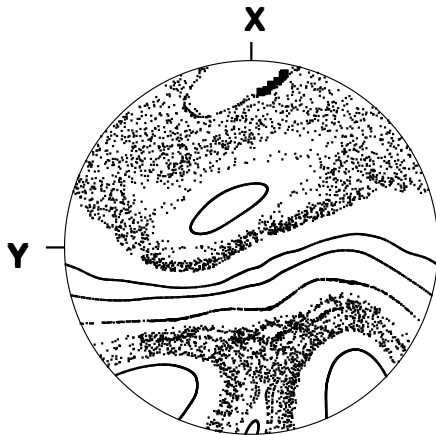


Fig. 4. First channel opening. Classical PM. Since Poincaré maps have a symmetry  $C_2$  around  $OX$ , only half the sphere is needed. We use a stereographic projection from  $+OZ$  of the lower part of the sphere. The open part is a small cap near the  $+OX$  axis. Large black squares at its border are ionizing trajectories.

To begin with, we select an energy just above the first threshold. As for the rest of this section we select  $L = 50$ ,  $J = 100$ ,  $2B = 10^{-10}$  a.u., so  $N$  varies between 50 and 150. As compared to the bound case, the ratio  $L/J$  has been increased from  $1/5$  to  $1/2$  to increase the transfer of energy between electron and core. The PM is given in Fig. 4. The ionization region corresponds to a very small white cap around the  $+OX$  axis. The large black squares at its border are the points of ionization of some trajectories.

The value of the phase shift  $\tau$  of the  $S$  matrix as a function of energy is shown in Fig. 5: for each energy there is only one open channel, thus one value of  $\tau$ .

The Husimi plot of the wave function at the first channel opening (see Fig. 6(a)) is located in the open part of the sphere. Resonances for nearly bound states appear as increments of  $\tau$  by one. The widths of the resonances vary widely. The physical reason for this is easily displayed by Husimi plots for the resonances observed in Fig. 5. The very broad resonance which spans all of Fig. 5 is seen to be localized in the chaotic region, overlapping widely with the open part of the sphere: Fig. 6(b). We see three other resonances of decreasing

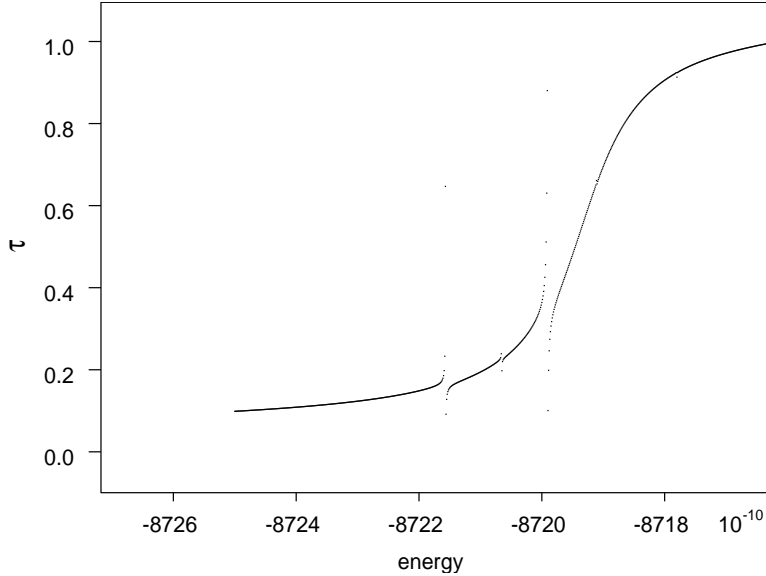


Fig. 5. First channel opening. Phase shift. It appears at the first ionization threshold, which is negative ( $-8726 \cdot 10^{-10}$ ), simulating a stray space charge: see text. There is only one phase shift  $\tau$ , because there is only one channel open, in this energy range. It increases by one for resonances between the open channel and some closed channels. Coupling  $\mu_{50} = 4$ .

width, which are also localized in the chaotic sea, but farther from the open part, as shown in Fig. 6(c)-(e). Note that these resonances live on the border of an integrable island, and are thus of similar type as states computed in ref. [36]. The state 6(f) is even narrower as it lives on or around an integrable island within this chaotic zone. It is seen as a one point glitch in Fig. 5. In addition there are much narrower resonances which cannot be found easily by the previous method. They are localized on or beyond the large regular region in the middle of the sphere, and have exceedingly small width, due to an exponentially small overlap of the Husimi function with the open part of the sphere.

Using the traditional method which looks for a zero value of a determinant we have been able to locate them by the following trick. We can set artificially a lower than zero threshold for ionization both in classical and in quantum mechanics: this would correspond to the existence of a long range screening potential, which might be due to stray electric fields or a space charge. In the classical simulation, this corresponds to considering an electron which after collision has an electronic energy higher than a given negative threshold  $E_{\text{thresh}}$  as ionized and not returning. In quantum mechanics, since the only difference between open and closed channels is the replacement of  $\nu_N$  by  $-\tau$ , this corresponds to performing this replacement for a finite value of  $\nu_N$ , which corresponds to this  $E_{\text{thresh}}$ . We have selected such a case: see the negative energy for opening of the first channel in Fig. 5. If we do not apply this trick, the whole sphere is closed for the same value of the parameters. We can thus

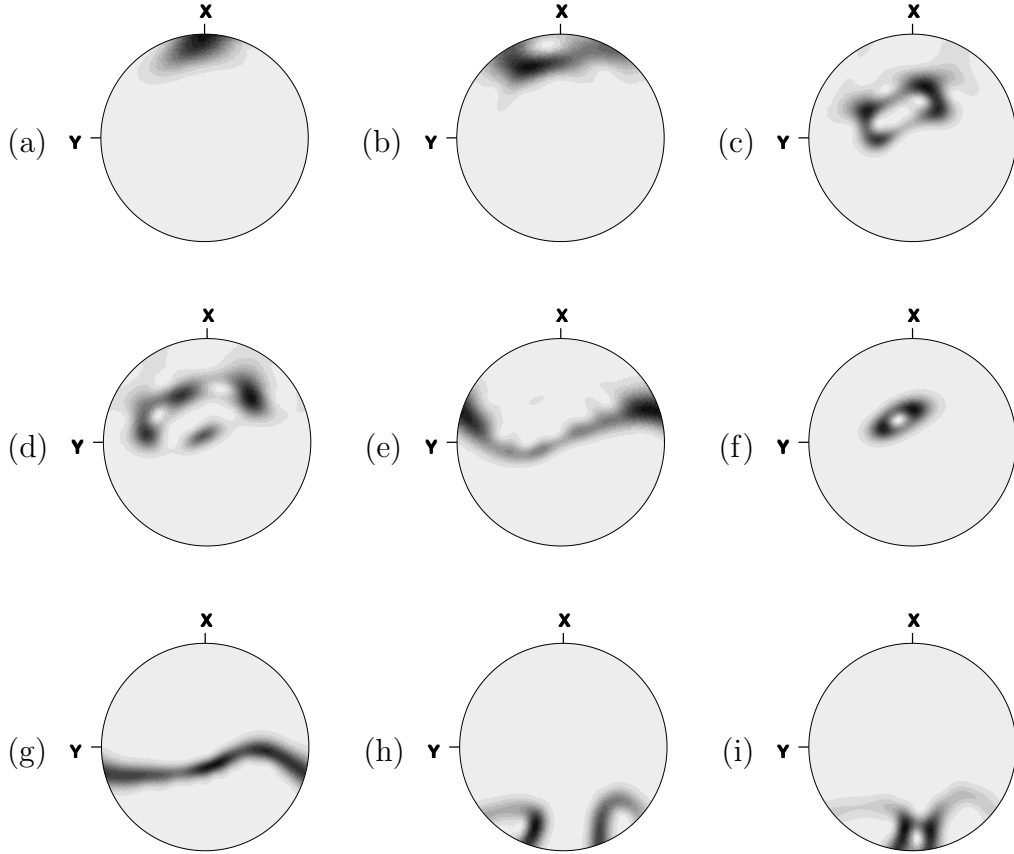


Fig. 6. First Channel Opening. Husimi plots of resonances. (a) Wave function of the open channel out of resonances. It is quantized on the open part of the sphere. (b): very large resonance which spans all Fig. 5, it has a large overlap with the open part of the sphere. (c)-(e) three narrow resonances seen in this figure (in order of decreasing widths) at  $-8.71991 \cdot 10^{-7}$  a.u. (width  $1.11 \cdot 10^{-12}$  a.u.),  $-8.72156 \cdot 10^{-7}$  a.u. (width  $2.26 \cdot 10^{-13}$  a.u.) and  $-8.72065 \cdot 10^{-7}$  a.u. (width  $3.15 \cdot 10^{-14}$  a.u.): they are located in the chaotic region connected to the open part. (f) the narrowest resonance seen in this figure, as only a one point glitch at  $-8.71780 \cdot 10^{-7}$  a.u. (width  $2.67 \cdot 10^{-15}$  a.u.): located on a regular island with some overlap with the chaotic sea. (g)-(h) extremely narrow resonances located in the regular regions: their widths are  $2 \cdot 10^{-21}$  and  $1.5 \cdot 10^{-29}$  a.u.. (i) an extremely narrow resonance located in the second chaotic sea between them. Its width is  $1 \cdot 10^{-27}$ , intermediate between the two previous ones, because it is separated from the open part by a regular region.

use MQDT for closed channels to compute energies and eigenfunctions of all channels. We select by inspection the wave functions quantized in the regular regions and run the open channel MQDT with a very small step to locate the resonances. Thus, we have been able to locate resonances of widths  $2 \cdot 10^{-21}$  and  $1.5 \cdot 10^{-29}$  a.u. located respectively in the regular regions near the equator and the bottom of the sphere, and also a resonance of intermediate width  $1 \cdot 10^{-27}$  located in the second chaotic sea between these two regular regions. In any case we have checked that the Husimi plots for the closed level and the resonance

are essentially equal, which provides a good check of our interpretation.

But this situation is quite unsatisfactory in the general case of truly positive energy, where we cannot use this trick to locate such narrow resonances. Fortunately the method of locating the poles of the  $\hat{S}$  matrix in the complex plane indicated at the end of section 3 is much more powerful. We can use the contour integration to locate the resonances by dichotomy in the complex plane, and finally use a root searching algorithm to compute them accurately once they have been approximately located. To check this method we have determined for example that the resonance at  $-8.71991 \cdot 10^{-7}$  a.u. (Figs. 5 and 6(c)) corresponds to a pole at complex energy value  $1.11 \cdot 10^{-12}$  a.u., consistent with the previous method, and that the resonance at  $-8.71780 \cdot 10^{-7}$ , seen as a one point glitch in Fig. 5 corresponds to a pole at complex energy value of  $2.67 \cdot 10^{-15}$  a.u. (Fig. 6(f)).

#### 4.4 Many Open Channels

We now increase the total energy to  $\sim 4.50 \cdot 10^{-7}$  a.u., such that slightly more than a half of the sphere is open. Ionization occurs in a cap around  $OX$  with  $\cos \alpha \gtrsim -0.1$ . We select two values of the coupling, a weak  $\mu_{50} = 0.4$  and a strong  $\mu_{50} = 9.81$ . The remaining parameters are chosen as  $L = 50$ ,  $J = 100$ ,  $2B = 10^{-10}$  a.u. as before.

##### 4.4.1 Weak coupling

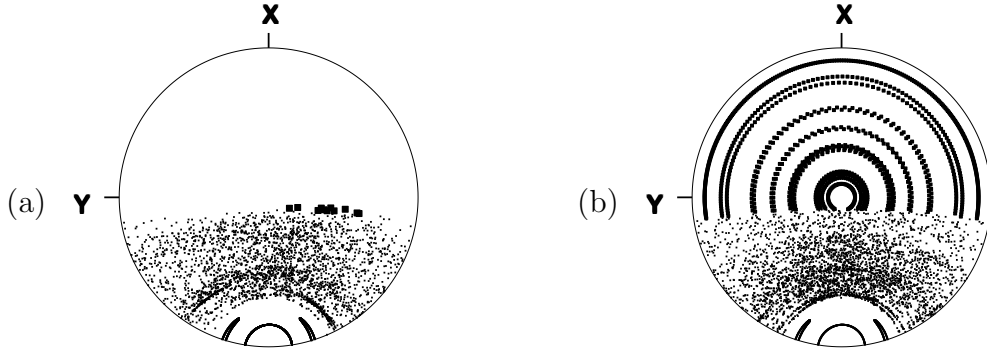


Fig. 7. Weak coupling. (a) Ordinary Poincaré Map. Iteration stops when the electron ionizes (black squares) (b) Combined Poincaré Jung map. When the electron ionizes iteration is continued with the Jung recipe (Fig. 1(b)). It follows circles on the open part of the sphere until it enters back into the closed part.

Fig. 7(a) displays the ordinary PM. Iteration stops when the electron ionizes (black squares) and a new trajectory is launched in the closed part of the

sphere. Fig. 7(b) shows the combined PM+JSM. Except for the regular islands near the  $-OX$  axis, it was obtained by running a single trajectory, i.e. using the PM for negative electron energies, and the JSM for positive energies. When the system is in the bound chaotic part it diffuses slowly towards the back or the front of the sphere. This diffusion mechanism was studied carefully in ref. [21]. When it ionizes, the JSM generates a set of one bounce events, tracing a semi circle around  $OZ$  in the open region, until it enters the bound region at the end of the semi circle and starts anew to diffuse. Due to the small value of  $\mu$  the number of steps needed to complete the semi circle is very large. The trajectory thus behaves like one injected very close to a parabolic manifold.

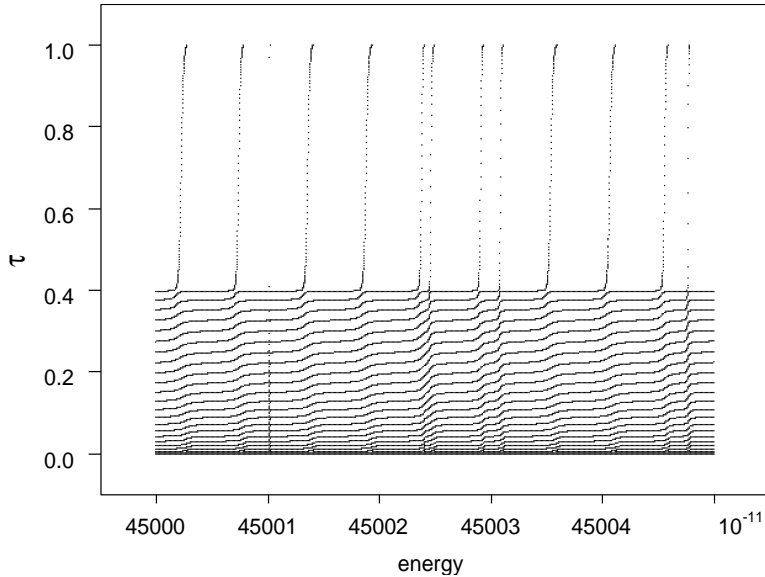


Fig. 8. Phase shifts. Weak coupling  $\mu_{50} = 0.4$

Quantum mechanically Fig. 8 displays the phase shifts for the eigenchannels. There are 23 channels open at this energy. We readily see that it displays a set of resonances.

Some Husimi plots of the eigenfunctions of the open channels are displayed in Fig. 9(a-c). They follow closely the trajectories of the JSM. In a previous letter we noted [15], that parabolic manifolds in a JSM may lead to eigenstates of the  $S$  matrix localized near this manifold (see also below). As we mentioned above the semicircles behave quite similarly, and as we do find states localized near these semi circles this again proves the applicability of the JSM to the description of the ionizing part of the spectrum in a semiclassical limit. Fig. 9(d) displays the Husimi plot of the first resonance seen in Fig. 8. It is quantized along the border of the regions of bound and unbound motion, yielding a large overlap with the open part resulting in a large width of the resonance. All resonances seen in Fig. 8 have similar Husimi plots. Functions lying further from the open channels would again correspond to extremely narrow resonances, which cannot easily be seen in the eigenphases with the

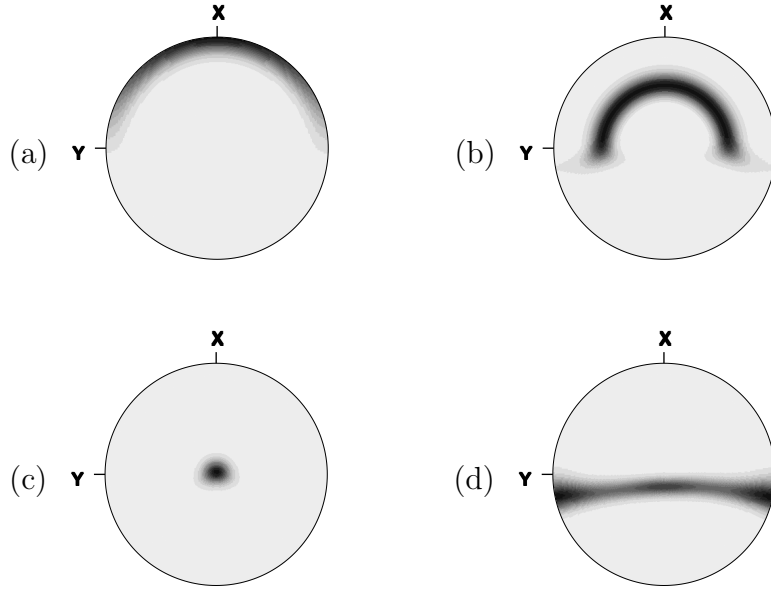


Fig. 9. Husimi plot of the MQDT eigenfunctions. Weak coupling. (a-c) Open channels are quantized along semi-circles which pertain to the Jung Map. (d) All resonances seen in Fig. 8 are quantized near the border of the separation between open and closed parts of the sphere.

present resolution.

#### 4.4.2 Strong coupling

Choosing as coupling strength  $\mu_{50} = 9.81$  the open part slightly greater than half a sphere. Fig. 10(a) shows the combined PM + JSM. Except for the fixed points described below all points of this combined PM + JSM pertain to a single trajectory. Due to the large value of the coupling this trajectory jumps randomly in and out of the bounded part within a few steps. The combined map is chaotic everywhere in this part. Fig. 11 displays the phase shifts. One sees a lot of avoided crossings between the phase curves, signaling a chaotic situation. A typical Husimi plot of an arbitrary wave function is shown in Fig. 10(b).

The important fixed points of this map (apart from isolated unstable fixed points embedded in the chaotic sea) are

- (i) the  $-OX$  axis in the bound part (PM) surrounded by a very small island of stability, too small with the present value of  $\hbar$  to capture a single quantum state.
- (ii) the  $\pm OZ$  axis in the open part surrounded by a larger regular island of the JSM. These are fixed points because the collision induces a rotation around  $OZ$ , entirely embedded in the open part (JSM).

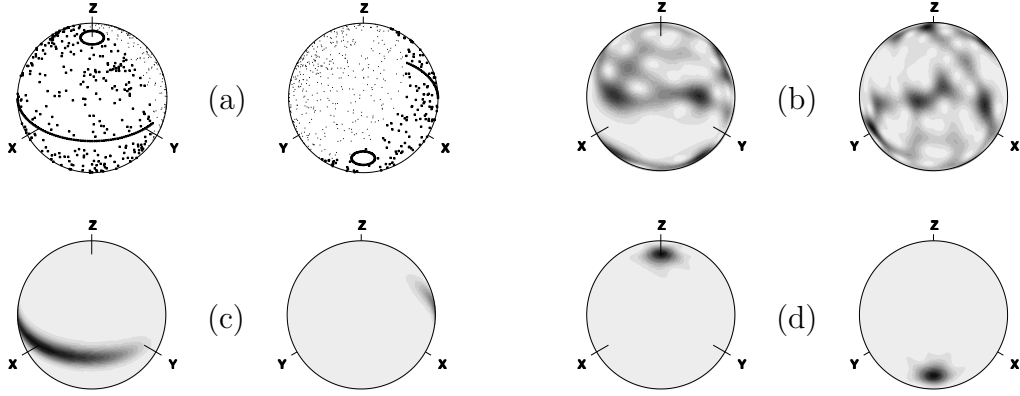


Fig. 10. Combination of PM and JSM. Strong coupling. Left: top view, right: bottom view. We do not use the stereographic projection as in Figs. 4, 7 because the parabolic manifold is badly seen with it. (a) Classical map. Small dots: PM, larger dots: JSM. The open part is slightly larger than half a sphere. The PM has only a very small island of stability at the back, too small to capture a quantum state with this value of  $\hbar$ . The JSM has two regular islands around  $\pm OZ$ , and the parabolic manifold of fixed points on the equatorial plane. All the remaining points lie in a single chaotic sea obtained with only one starting point, iterated by the PM when bound, and by the JSM when ionized. (b) Husimi plot of a typical arbitrary state: it extends randomly over the whole sphere (c) Husimi plot of a quantum state quantized on the parabolic manifold. (d) Husimi plot of a quantum state quantized on the  $\pm OZ$  cap.

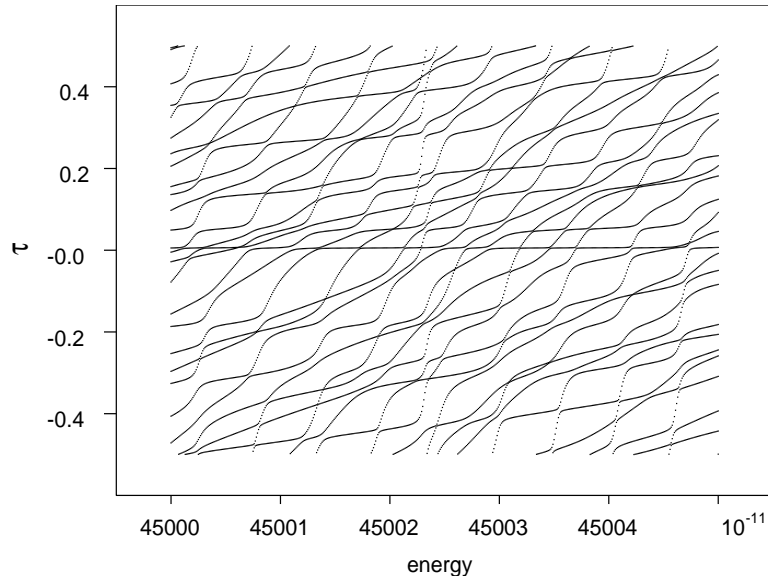


Fig. 11. Eigenphases as a function of energy. Strong coupling  $\mu_{50} = 9.81$

- (iii) all points in the equatorial plane in the open part (JSM). An electron entering the collision region with  $\theta_L = \pi/2$  and arbitrary  $\varphi_L$ , up to the restriction that the electron energy should be positive, will emerge from the collision region with the same angular momentum direction because

the increment  $\delta\varphi_L = K \cos\theta_L$  equals zero. We thus have a parabolic manifold of fixed points.

- (iv) if  $|K|$  is chosen larger than  $n \cdot 2\pi$ , that is  $\mu_L > \frac{nL}{2}$  we would also find lines mapped onto themselves at angles  $\theta_L$  corresponding to  $K \cos\theta_L = 0, \pm 2\pi, \dots, \pm n \cdot 2\pi$

In particular the parabolic manifold is embedded in the chaotic sea. A nearly horizontal curve may be observed in the middle of Fig. 11. It corresponds to the fixed points of this parabolic manifold in the equatorial plane as shown by Fig. 10(c)(see also ref. [15]). For e.g. the stadium billiard, such manifolds of fixed points embedded in a chaotic sea have significant quantum effects. There they give rise to the so called bouncing ball states which in turn lead to deviations of the spectral fluctuation properties in the eigenvalue spectrum from the random matrix results [37]. We expect similar quantum effects of the parabolic manifolds on statistical properties of the eigenphases of the scattering matrix. When considering eigenphases of the scattering matrix as a function of the energy  $E$  or the coupling strength  $\mu_L$ , we find eigenphases which merely change. The other fixed point near the  $\pm OZ$  poles, surrounded by a significant island of stability in the JSM, is less conspicuous in Fig. 11. It corresponds to a horizontal line near  $\tau = -0.3$ , barely visible due to strong avoided crossings. It nevertheless traps a quantum state as seen in Fig. 10(d).

## 5 Comparison between semi-classical and quantum evolution on the surface of section

### 5.1 Principle

We want to compare our results with the original work of Bogomolny [9,10,11], which was based on the semi-classical formula

$$T(\varphi, \varphi') = \sum_{\text{cl.tr.}} \sqrt{\frac{\partial^2 S(\varphi, \varphi') / \partial\varphi\partial\varphi'}{-2\pi i\hbar}} \exp\left(\frac{i}{\hbar} S(\varphi, \varphi')\right), \quad (36)$$

where, as in the remainder of this section, we use the notations of the review paper of W.H. Miller [38]. In particular the  $i$  and the signs in the argument of the square root function take care of the Maslov index.

We first notice that the simple minded way of using this equation, computing  $S = \int pdq$  using the formulae obtained in the previous classical part of this paper and the previous ones does not work, because our “classical” molecular reference frame is a moving frame, implying that  $L_{Z_C}$  is not conjugate to  $\varphi_L^C$ . Indeed consider first the collision step. The change of orientation of  $\mathbf{L}$  in this

frame entails, by conservation of angular momentum, a change of the orientation of  $\mathbf{N}$ , and thus of the orientation of this frame, by an angle called  $\delta\varphi'_L$  in section 2 and  $\varphi'_N$  in Appendix A.1. This extra rotation of the frame implies that  $L_{Z_C}$  is no longer the generator of rotations of  $\varphi_L^C$  around the  $OZ_C$  axis. For the collision step this problem can be solved by using the “quantum” molecular reference frame, which is fixed, since the collision is taken as instantaneous, and that this frame is obtained from the laboratory frame by a rotation with fixed Euler angles  $\varphi_M, \theta_M, 0$  (see Appendix A). That this analysis is correct is shown by noting that the transformation produced by the collision in the “quantum” reference frame  $\delta\varphi_L^Q = K \cos\theta_L^Q$  is canonical (the exterior differential product  $dL_{Z_Q} \wedge d\varphi_L^Q$  is conserved), while the corresponding for the “classical” frame quantities is not. Moreover the transformation from the “quantum” to the “classical” molecular reference frame is not canonical as shown in Appendix A.1, where we have computed the momentum conjugate to  $\varphi_L^C$ , such that this transformation becomes canonical (eq. A.7). Nevertheless, since our goal is physical evidence we prefer to stick to our previous practice of using  $L_{Z_C}, \varphi_L^C$ . The only drawback of using non canonical coordinates is that the map is not area preserving on the sphere, a minor effect for  $L/J = 1/5$  or  $1/2$  as chosen in this paper.

For the collision step we thus can solve this problem by using the “quantum” molecular frame, but the problem reappears for the Coulomb step, where this frame is also moving. We could compute everything in the laboratory frame, but it is more meaningful to use the “quantum” molecular frame for the collision step, the laboratory frame for the Coulomb step, and two semiclassical formulae for the change between these coordinate frames. This procedure follows closely the purely quantum formulation, giving a semiclassical approximation for each of the steps which enter in the discussion of section 3, as shown in Table 1. It provides direct evidence that MQDT indeed is the exact quantization of the Bogomolny formulation, in particular that eqs. (26, 35) are the exact counterpart of the semi classical eq. (1.20) of ref. [10], remembering that  $\hat{\mathcal{E}}$  describes half a turn, while  $T$  describes a full turn.

As Poincaré section we select in coordinate space the intersection at radius  $r_0$  with outgoing trajectories, i.e. an “after collision” Poincaré map. We thus write:

$$T = U^c U^{QL} U^f U^{LQ} \quad (37)$$

where from right to left the  $U^i$ 's indicate the unitary semiclassical operators for the transformation from the “quantum” molecular reference frame to the laboratory frame, free motion in the laboratory frame, back to the “quantum” molecular frame and collision in the “quantum” frame. All these operators are built with  $F_2 / F_3$  kind of generating functions, i.e. they are of the form

$$\begin{aligned}
(U\psi)(\varphi) &= \iint \sqrt{\frac{\partial^2 F_3(I', \varphi)/\partial I' \partial \varphi}{2\pi i \hbar}} \exp\left(\frac{i}{\hbar}(F_3(I', \varphi))\right) \\
&\quad \times \sqrt{\frac{-1}{2\pi i \hbar}} \exp\left(-\frac{i}{\hbar}I'\varphi'\right) \\
&\quad \times \psi(\varphi') dI' d\varphi'
\end{aligned} \tag{38}$$

where  $I'$  is the momentum conjugate to the coordinate  $\varphi'$  and the resulting integral is evaluated with the stationary phase approximation. This generating function is of type  $F_3$  as it is a function of the old momentum  $I'$  and the new coordinate  $\varphi$ . An auxiliary Fourier transform is used to go from old coordinate  $\varphi'$  to old momentum  $I'$ . Evaluating the inner  $dI'$  integral by the stationary phase approximation amounts to computing an  $F_1$  type generating function, and inverting the order of the Fourier transform and of the  $F$  integral amounts to defining an  $F_2$  generating function. Note that we have defined by this double integral a  $U$  operator which goes from coordinate  $\varphi'$  to coordinate  $\varphi$  representation, while the  $F_3$  integral on its own gives an operator from the old momentum  $I'$  to the new coordinate  $\varphi$ . Hence, we can compute eq. (37) by performing four integrations instead of eight by alternating between the coordinate and the momentum representations. We can compute with the same procedure a momentum coordinate  $T_{\Lambda\Lambda'}$  matrix by simply introducing two Fourier Transforms to the left and the right of the operator  $T$ . As momenta are quantized  $T_{\Lambda\Lambda'}$  depends on discrete variables, while  $T(\varphi, \varphi')$  is a function of continuous arguments. If there are no singularities all these possibilities give the same result. We shall use them freely in order to obtain generating functions which we can compute analytically and we shall see in section 5.3 that this choice offers possibilities to circumvent singularity problems.

## 5.2 Computations

First notice that the conjugate pair of coordinates in the “quantum” molecular frame is the known  $\{L_{Z_Q}, \varphi_L^Q\}$  pair. The momentum in the laboratory frame is the modulus  $N$  of  $\mathbf{N}$ . Intuitively the conjugate angle is the angle  $\varphi_N$  of rotation of the core axis  $\hat{\mathbf{M}}$  around  $\mathbf{N}$ , referred to a reference axis which only can be  $\mathbf{J}$ . Explicit formulae for computing the transformation are given in Appendix A.2, where we also show that the transformation from  $\{L_{Z_Q}, \varphi_L^Q\}$  to  $\{N, \varphi_N\}$  is indeed canonical, justifying our intuition concerning the definition of  $\varphi_N$ .

The computation of the  $F_3$  generating functions for the collision and the free rotation steps follows the same scheme. In both cases the momentum is conserved, while the angle is increased by an amount which is a function of the corresponding momentum  $I$  only  $\delta\varphi = f(I)$ , respectively  $\delta\varphi_L^Q = KL_{Z_Q}$  and  $\delta\varphi_N = -\delta\beta = +2\pi T_e/T_N$  (the free rotation is direct in the laboratory frame

and seen with inverse orientation in the “classical” molecular frame), which is a function of  $N$  only for a given total energy  $E$ . Using the equations defining  $F_3(I', \varphi)$ , namely  $\varphi' = \partial F_3 / \partial I'$  and  $I = \partial F_3 / \partial \varphi$  we obtain

$$F_3(I', \varphi) = \varphi I' - \int f(I') dI' \quad (39)$$

i.e. using [8, eqs. (A11,A12)]:

$$\begin{aligned} F_3(L'_{Z_Q}, \varphi_L^Q) &= L'_{Z_Q} \varphi_L^Q - K \frac{L'_{Z_Q}{}^2}{2L} = L'_{Z_Q} \varphi_L^Q + 2\pi \mu_{L'_{Z_Q}} \\ F_3(N', \varphi_N) &= N' \varphi_N + 2\pi \nu_{N'} \end{aligned} \quad (40)$$

The computation of the  $F_2$  or  $F_3(L_{Z_Q}, \varphi_N)$  is more tricky. First, whether it is a  $F_2$  or  $F_3$  generating function depends on which is the original and the new frame, and we need both transformations. To go in the opposite direction we use the unitarity of the operator  $U$ . We start with the following formula which expresses  $N$  as a function of the independent variables:

$$N = \left| \sqrt{J^2 - (L_{Z_Q} / \sin \varphi_N)^2} \pm \sqrt{L^2 - (L_{Z_Q} / \sin \varphi_N)^2} \right| \quad (41)$$

This formula can be computed analytically by eliminating  $\varphi_L^Q$  between eqs. (A.11) and (A.15) and using eq. (A.13). It is more satisfying to notice that a little geometrical thinking on Fig. 2(b) shows that it results from projecting the  $J$  and  $L$  sides of the triangle given by the relation  $\mathbf{J} = \mathbf{L} + \mathbf{N}$  onto the  $N$  side, because the common height is equal to  $|L_{Z_Q} / \sin \varphi_N|$ . By integration over  $\varphi_N$  we obtain

$$\begin{aligned} F_2(L_{Z_Q}, \varphi_N) &= \left( L_{Z_Q} \text{ArcXY} \left( \sqrt{J^2 - (L_{Z_Q} / \sin \varphi_N)^2}, L_{Z_Q} \cot \varphi_N \right) \right. \\ &\quad \left. + J \text{ArcXY} \left( J \cos \varphi_N, \sqrt{J^2 - (L_{Z_Q} / \sin \varphi_N)^2} \sin \varphi_N \right) \right) \\ &\quad \pm \left( L_{Z_Q} \text{ArcXY} \left( \sqrt{L^2 - (L_{Z_Q} / \sin \varphi_N)^2}, L_{Z_Q} \cot \varphi_N \right) \right. \\ &\quad \left. + L \text{ArcXY} \left( L \cos \varphi_N, \sqrt{L^2 - (L_{Z_Q} / \sin \varphi_N)^2} \sin \varphi_N \right) \right) \end{aligned} \quad (42)$$

where ArcXY is an unambiguous notation for the angle of a vector whose projections on the  $X$ - and  $Y$ -axes are known (the order of parameters for the analogous atan2 used in some programming languages is not fixed).

Notice that the derivative of  $F_2$  with respect to  $L_{Z_Q}$ , which must give  $\varphi_L^Q$ , equals the sum of the coefficients of  $L_{Z_Q}$  in the first and third terms of eq. (42) (this also has a geometrical interpretation). This shows that the sum of these terms is precisely equal to  $\varphi_L^Q L_{Z_Q}$ . Using this result we can solve the problem

of the integration constant depending on  $L_{Z_Q}$ , which appears in the integration over  $\varphi_N$ . We follow continuously the various angles over ranges greater than  $2\pi$  during the computations in order to compute the exact values of the various  $\text{ArcXY}$ .

Next we compute the actions  $S(\varphi, \varphi')$  and  $S(\Lambda, \Lambda')$ . We start from a pair of conjugate  $\{L'_{Z_Q}, \varphi_L^{Q'}\}$ , i.e. a point on the Poincaré sphere, and compute analytically the final  $L_{Z_Q}, \varphi_L^Q$  as a function of these. To compute, say  $S(\varphi_L^Q, \varphi_L^{Q'})$ , we first invert numerically the relation between  $\varphi_L^Q$  and  $L'_{Z_Q}$  for fixed  $\varphi_L^{Q'}$ . Usually, there are several solutions. For each solution we then compute  $S$  as a function of  $\varphi_L^{Q'}$  and  $L'_{Z_Q}$  by adding the various  $F_n$  generating functions which enter in the exponentials of the  $U$  operators which are used to build  $T$ .

We do not need to evaluate all intermediate integrals by stationary phase to obtain the amplitudes. Indeed, it was shown in ref. [38] that the formula for the amplitude given in eq.(36) is a direct consequence of the action being a  $F_1$  generating function of a canonical transformation between the initial and the final states. We thus only need to compute the second derivative of  $S$  with respect to  $\varphi_L^Q$  and  $\varphi_L^{Q'}$ . For this we use the derivatives of  $S$  with respect to initial variables  $L'_{Z_Q}$  and  $\varphi_L^{Q'}$ , that we have computed analytically by following the various steps, and general calculus formulae for second derivatives of inverse functions. We have checked that these amplitudes obey the relationship,

$$\left| \frac{\partial^2 S(\varphi_L^Q, \varphi_L^{Q'})}{\partial \varphi_L^{Q'} \partial \varphi_L^Q} \right| = \left| \left( \frac{\partial \varphi_L^Q}{\partial L'_{Z_Q}} \right)_{\varphi_L^{Q'}} \right|^{-1} \quad (43)$$

which was shown in ref. [38, eq. (2.54b)] to be a simple consequence of the conservation of probability. This is a very useful test of our way to compute  $S$  since the second term of this equation does not depend on  $S$ .

### 5.3 Singularities in the semi classical computations

We then use the resulting  $T(\varphi, \varphi')$  and  $T(\Lambda, \Lambda')$  to compute the evolution of wave packets as was done in section 4.2. The first problem which appears is the existence of divergences of the amplitudes. Fig. 12 plots the amplitudes of  $T$  as a function of the initial position on the Poincaré sphere, which was used as a first step to compute them. The black lines of maxima are actually divergences. They are at different positions for the two representations.

The physical meaning of these divergences is the existence of focus singularities. We discuss the  $\varphi$  representation first, by referring to Fig. 13(a). Various trajectories starting from the same coordinate point with different momenta

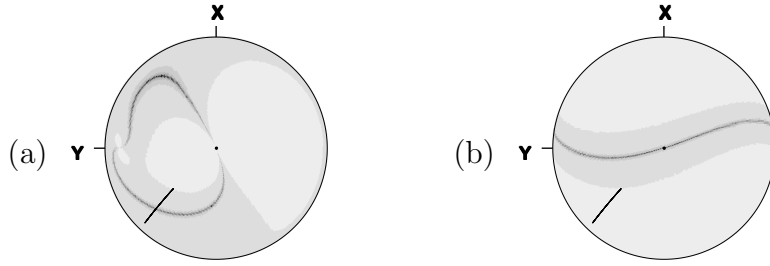


Fig. 12. Divergence of the semiclassical amplitudes. (a)  $T(\varphi, \varphi')$ . (b)  $T(\Lambda, \Lambda')$ . The part of a straight line going through the  $OZ$  pole in the lower left of the sphere is the input corresponding to Fig. 13(b): the fact that it is slightly distorted is due to plotting in the “classical” reference frame instead of the “quantum” reference frame.

refocus at the same point (on the map). On the sphere the coordinate is  $\varphi'$  and the momentum is  $L'_Z$ . The points aligned on the straight line in the lower left part of Fig. 12(a) and (b), have the same value of  $\varphi'$  and a varying  $L'_Z$ . They thus constitute a fan of initial trajectories. The image of this line is given in Fig. 13(b). The focus is caused by the folding part of this image, precisely the point where it is tangent to a radius from the  $OZ$  pole: same position  $\varphi$  independent to first order of the initial momentum  $L'_Z$ . The divergence of the amplitude is a consequence of the presence of the term  $\partial\varphi/\partial L'_Z|\varphi'$  in the denominator of the second part of eq. (43).

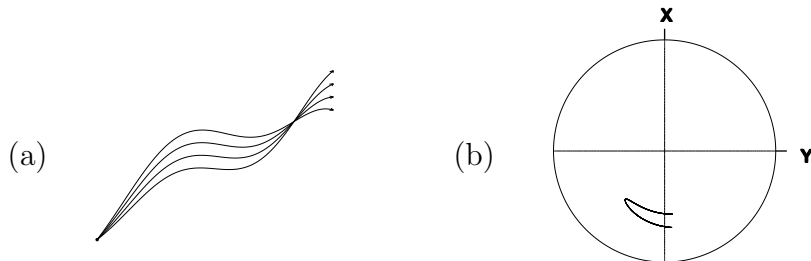


Fig. 13. Focus singularities. (a) represents such a singularity in an ordinary (flat) coordinate space. (b) plots the image of the straight oblique line in the lower left part of Fig. 12 (a) and (b) which cross the singularity line in the  $T(\varphi, \varphi')$  representation. All starting points on this segment have the same coordinate  $\varphi'$ , but different momenta  $L'_Z$ , i.e. they are equivalent to the starting points in (a). The back folding of the image in (b), common especially to chaotic situations, is the cause of the focus singularity: see text.

The problem of singularities is common in any semi classical analysis. Their solution, usually called “regularization” follow two main routes. The first, common in physics textbooks, is to revert to a full quantum computation near the singular point, and to match the results with the semi classical computation distant from it. Notice that the MQDT analysis is such a fully quantum so-

lution. The second, common in some mathematical works, is to notice that we can circumvent the problem by changing from coordinate to momentum representation through a Fourier transform. The singularity is a result of a projection from phase space onto coordinate space; there are no singularities in phase space itself. The back bending in Fig. 13(b) which is tangent to a meridian of the sphere is not tangent, at this point, to a parallel. The starting points in Fig. 12 which project onto the same  $\varphi'$  project to different  $L'_Z$ . The lines of singularities exist in both representations in Fig. 12, but they appear at different points. So one can compute the points of the map by different routes, a possibility rooted on the possible choice at each  $U$  step in the computation of  $T$  (eq. (37)) to select the  $\varphi$  or  $L_Z$  representation, both in the initial and the final state. The only remaining problem is the fact that both lines of singularities share the  $\pm OZ$  poles. To solve it we would have to use a more general change of canonical coordinates on the sphere, a rotation which can change the position of the poles. We do not attempt to do this in the present paper.

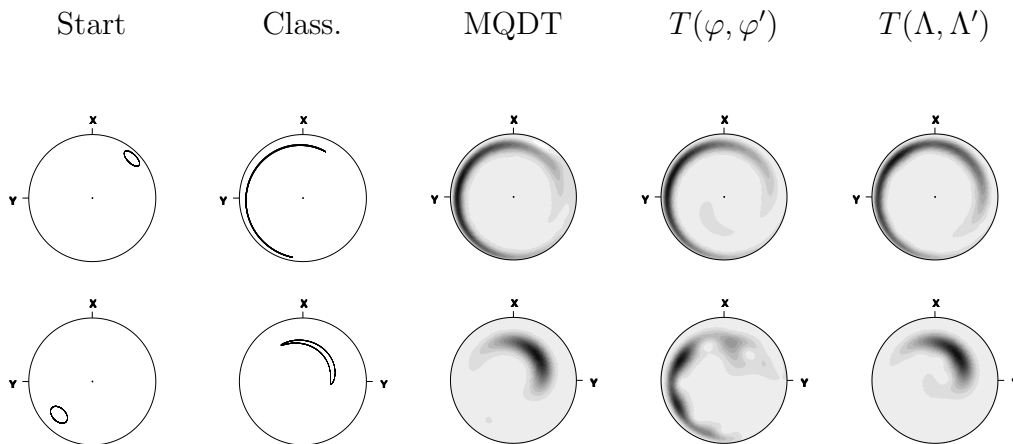


Fig. 14. Effect of focus singularities. The starting points lie on a circle. We show the first iteration by the Poincaré map, and the corresponding Husimi plots with different techniques. First row: starting in a point without singularity. Second row: starting in a point with a  $\varphi$  focus singularity, at the intersection of the circle with the straight line in the lower left part of Fig. 12(a) and (b) and the singularity line in the  $\varphi$  representation.

Illustration of this is given in Fig. 14. The starting point in the first row is selected to correspond to no singularity in any of the two representations. All computations, classical, quantum and semi classical in both representations agree nicely. In the second row the starting point lies on the singular line in the  $\varphi$  representation, but on a regular point in the  $\Lambda$  representation. The result of the  $T(\varphi, \varphi')$  computation is highly distorted, while that of the  $T(\Lambda, \Lambda')$  computation agree nicely with classical and MQDT computations.

## 6 Conclusion

We have formulated the multichannel quantum defect theory for Rydberg molecules as the quantization of a classical symplectic map composed of a standard surface of section for negative electron energies and a Jung scattering map for positive ones. This formulation elucidates MQDT from an entirely different point of view. Simultaneously we have shown it to provide considerable computational advantages.

The method was applied in the context of a simplified model, where only one rotational degree of freedom for the molecule was taken into account. Simultaneously, the absolute value of the electron angular momentum was fixed. This approximation allows for a two dimensional surface of section, and simplified calculations, but is *not* essential to the representation of MQDT as a quantum Poincaré map. These applications demonstrate the simplifications achieved. Finally we establish the relation to Bogomolny's [9,10,11] semi classical formulation of the quantum Poincaré map. Considering caustics we can clearly see the basic difference between the exact and the semi-classical map.

## A Reference Frames

We use three reference frames, the laboratory reference frame  $Oxyz$ , and two molecular reference frames, called "Classical"  $OX_C Y_C Z_C$  and "Quantum"  $OX_Q Y_Q Z_Q$  molecular reference frames.

In purely classical computations the "Classical" right handed molecular reference frame is defined in such a way that  $OZ_C$  lies along the inter nuclear axis  $\hat{\mathbf{M}}$  of the molecular ionic core, and  $OX_C$  lies along its angular momentum  $\mathbf{N}$ . This is adequate because the two steps of the dynamics, namely the collision and the free rotation, are rotations about these two axes. We always use it to display our results, as the physical content is most obvious within this frame.

However, this is not the molecular reference frame selected in usual definitions of quantum wave functions. There the molecular frame  $OX_Q Y_Q Z_Q$  is defined as the one deduced from the laboratory frame  $Oxyz$  by a rotation of three Euler angles (with the conventions of [18]). The first two are well defined, namely  $\varphi_M$ ,  $\theta_M$ , the polar angles of  $\hat{\mathbf{M}}$ . The third is arbitrary for a diatomic molecule, since it corresponds to a rotation around the molecular axis. It is given an arbitrary value 0 or  $\pi/2$ , depending on authors; we will select 0 as in [2].

Both reference frames share the same  $OZ = \hat{\mathbf{M}}$  axis, but have different  $OX$

axes. The classical  $OX_C = \mathbf{N}$  axis is not well defined in quantum mechanics, since  $\mathbf{N}$  is a momentum conjugate to the angles  $\varphi_M$ , and  $\theta_M$ , which are the variables defining the rotational molecular wave function in eqs. (2-3). Thus the classical reference frame defines the usual quantum wave functions only in the semi classical limit. But conversely, the quantum reference frame is also well defined in classical mechanics. So, if we want to compare classical and quantum results, we do the quantum calculations in the usual quantum reference frame, and then plot the resulting Wigner or Husimi distributions in the classical reference frame, by applying the well defined classical rotation which brings the quantum reference frame onto the classical one.

We shall now compute the formulae which connect these three frames. They are based on the fact that we can compute the position of  $\mathbf{J}$  and  $\mathbf{N}$  in  $OX_QY_QZ_Q$  once we know the position of  $\mathbf{L}$  in this frame, using simple geometrical relations: see Fig. 2(b). We first need to define precisely the laboratory reference frame. Since everything is invariant with respect to a rotation of the whole space, we may choose the  $Oz$  axis along  $\mathbf{J}$  (Fig. 2(a)). Quantum mechanically this amounts to studying the  $|J, M_J\rangle = |J, J\rangle$  state. Conversely, once we know the position of  $\mathbf{J}$  in the molecular frame, we know the position of the  $Oz$  axis of the laboratory frame in  $OX_QY_QZ_Q$ , but there is no way to locate the  $Ox$  and the  $Oy$  in this molecular frame. This is a consequence of the rotational invariance of the problem. The corresponding angle  $\varphi_M$  is conjugate to  $J_z$ , and is one of the variables we have eliminated when reducing the dimension of phase space from 10 to 4 (or 6 if  $L$  is not kept constant).

The position of  $\mathbf{J}$  in  $OX_QY_QZ_Q$  is a simple consequence of our choice of 0 as the third Euler angle of the rotation which brings the laboratory frame  $Oxyz$  onto the ‘‘Quantum’’ molecular reference frame  $OX_QY_QZ_Q$ . These three Euler angles are  $\varphi_M$ ,  $\theta_M$ , and 0. The first Euler rotation of the angle  $\varphi_M$  keeps  $\mathbf{J} = Oz$  fixed and brings  $Oy$  onto  $OY_Q$ . The second Euler rotation around  $OY_Q$  by an angle  $\theta_M$  brings  $Oz$  onto  $OZ_Q$ . Conversely the position of  $\mathbf{J}$  in the molecular frame is obtained by a rotation of  $-\theta_M$  around  $OY_Q$ . It is thus located in the  $OX_QZ_Q$  plane with coordinates  $J_{X_Q} = -J \sin \theta_M$ ,  $J_{Y_Q} = 0$ ,  $J_{Z_Q} = J \cos \theta_M$ , always directed towards negative  $OX_Q$  since  $0 \leq \theta_M \leq \pi$ .

### A.1 Transformations between ‘‘Classical’’ and ‘‘Quantum’’ molecular frames

Let us compute  $\mathbf{N}$  in  $OX_QY_QZ_Q$ . For a diatomic molecule, the momentum  $\mathbf{N}$  is perpendicular to the inter nuclear axis  $\hat{\mathbf{M}}$ , since the moment of inertia around the inter nuclear axis is zero. Thus  $\mathbf{N}$  is in the  $OX_QY_Q$  plane. We then write  $\mathbf{N} = \mathbf{J} - \mathbf{L}$  in this frame

$$\begin{aligned}
N_{X_Q} &= -J \sin \theta_M - L \sin \theta_L^Q \cos \varphi_L^Q \\
N_{Y_Q} &= 0 - L \sin \theta_L^Q \sin \varphi_L^Q \\
N_{Z_Q} &= J \cos \theta_M - L \cos \theta_L^Q
\end{aligned} \tag{A.1}$$

$N_{Z_Q} = 0$  leads to

$$\begin{aligned}
\cos \theta_M &= \frac{L}{J} \cos \theta_L^Q \\
\sin \theta_M &= +\sqrt{1 - \cos^2 \theta_M},
\end{aligned} \tag{A.2}$$

because  $0 \leq \theta_M \leq \pi$ . This gives the position of  $\mathbf{J}$  once  $\mathbf{L}$  is known in  $OX_QY_QZ_Q$ . Then  $\mathbf{N}$  lies in the plane  $OX_QY_Q$  at an angle

$$\begin{aligned}
\varphi_N^Q &= \text{ArcXY} (N_{X_Q}, N_{Y_Q}) \\
&= \text{ArcXY} \left( -\sqrt{J^2 - L^2 \cos^2 \theta_L^Q} - L \sin \theta_L^Q \cos \varphi_L^Q, -L \sin \theta_L^Q \sin \varphi_L^Q \right)
\end{aligned} \tag{A.3}$$

where we have used eqs. (A.1) and (A.2), and where ArcXY is defined after eq. (42).

Thus the “quantum” molecular reference frame angles for  $L$  are related to their corresponding “classical” reference frame value via:

$$\begin{aligned}
\theta_L^C &= \theta_L^Q \\
\varphi_L^C &= \varphi_L^Q - \varphi_N^Q
\end{aligned} \tag{A.4}$$

The reverse is not obtained by simply inverting this relation. We rather express the relation  $\mathbf{J} = \mathbf{N} + \mathbf{L}$  in the “classical” reference frame, where we know that  $\mathbf{N}$  is along  $OX_C$ .

$$\begin{aligned}
J_{X_C} &= N + L \sin \theta_L^C \cos \varphi_L^C \\
J_{Y_C} &= +L \sin \theta_L^C \sin \varphi_L^C \\
J_{Z_C} &= +L \cos \theta_L^C
\end{aligned} \tag{A.5}$$

Since the  $OZ$  axis is common in the “quantum” and “classical” molecular reference frames, relations A.2 are conserved with  $\theta_L^Q$  replaced by  $\theta_L^C$ . Then we recall that in the  $OX_QY_QZ_Q$  reference frame the projection of  $\mathbf{J}$  into the  $OX_QY_Q$  plane, which is identical with the  $OX_CY_C$  plane, is always directed

along the negative  $OX_Q$  axis, which locates the  $OX_Q$  axis in the “classical” frame. Thus

$$\begin{aligned}\varphi_L^Q &= \varphi_L^C - \text{ArcXY} \left( -N - L \sin \theta_L^C \cos \varphi_L^C, -L \sin \theta_L^C \sin \varphi_L^C \right) \\ &= \varphi_L^C - \text{ArcXY} \left( -\sqrt{J^2 - L^2(1 - \sin^2 \theta_L^C \cos^2 \varphi_L^C)}, -L \sin \theta_L^C \sin \varphi_L^C \right)\end{aligned}\quad (\text{A.6})$$

where the second line is obtained by using eq. (1) which was written in the “Classical” molecular frame.

Finally notice that the transformation between  $\{ L_{Z_Q}, \varphi_L^Q \}$  and  $\{ L_{Z_C}, \varphi_L^C \}$  is not canonical, as can be checked by mere differentiation from the non conservation of  $dL_Z \wedge d\varphi_L$  (where  $\wedge$  denotes the exterior differential product). We have computed a generating function, and it can be checked by differentiation that a momentum conjugated to  $\varphi_L^C$  would be

$$\begin{aligned}I(\varphi_L^C, \theta_L) &= L \cos \theta_L + \\ &\frac{(J^2 - L^2) \mathbf{F} \left( \frac{\pi}{2} - \theta_L, \frac{L^2 \cos^2 \varphi_L^C}{J^2 - L^2 \sin^2 \varphi_L^C} \right) - (J^2 - L^2 \sin^2 \varphi_L^C) \mathbf{E} \left( \frac{\pi}{2} - \theta_L, \frac{L^2 \cos^2 \varphi_L^C}{J^2 - L^2 \sin^2 \varphi_L^C} \right)}{\cos \varphi_L^C \sqrt{J^2 - L^2 \sin^2 \varphi_L^C}}\end{aligned}\quad (\text{A.7})$$

where  $\mathbf{E}$  and  $\mathbf{F}$  are elliptic functions, instead of  $L_Z^C = L_Z^Q = L \cos \theta_L$ . It can be checked that the extra term vanishes when  $L/J \ll 1$ , as it should do since in this case the frame recoil is negligible. The effect is thus small in this paper where we have selected  $L/J = 1/5$  or  $1/2$ . But this formula is too unwieldy to be of any use, especially since our main goal in using “classical” reference frame coordinates is physical visualizing of the results.

## A.2 Transformation between “Quantum” molecular reference frame and laboratory reference frame

The canonical momentum and angle in the “quantum” molecular reference frame are  $L_{Z_Q}$  and  $\varphi_L^Q$ . The canonical momentum and angle in the laboratory frame (for the reduced phase space) are  $N$  and its conjugate angle  $\varphi_N$ , to be defined, and not to be confused with  $\varphi_N^Q$  (eq. A.3), which is the angle of  $\mathbf{N}$  in the plane  $OX_QY_Q$ . We first express  $N$  as a function of “quantum” molecular coordinates (eq. (1) was with “classical” molecular coordinates). Using eqs. (A.1, A.2) we obtain

$$N^2 = J^2 + L^2 - 2L_{Z_Q}^2 + 2\sqrt{L^2 - L_{Z_Q}^2}\sqrt{J^2 - L_{Z_Q}^2}\cos\varphi_L^Q\quad (\text{A.8})$$

Intuitively (we will justify it below) the angle conjugate to  $N$  is the angle  $\varphi_N$

of rotation of the molecular axis  $\hat{\mathbf{M}}$  around  $\mathbf{N}$ . The reference for this angle can only be the position of  $\mathbf{J}$ . Notice that the relative positions of  $\mathbf{J}$  and  $\mathbf{N}$  have nothing special. We choose as reference axis around  $\mathbf{N}$  the unit normal  $\mathbf{n}$  to the plane  $\{\mathbf{N}, \mathbf{J}\}$ :

$$\mathbf{n} = \frac{\mathbf{N} \times \mathbf{J}}{|\mathbf{N} \times \mathbf{J}|} = \frac{\mathbf{L} \times \mathbf{J}}{|\mathbf{L} \times \mathbf{J}|} \quad (\text{A.9})$$

(using  $\mathbf{N} = \mathbf{J} - \mathbf{L}$ ,  $\times$  denotes the skew vector product) and the unit binormal

$$\mathbf{m} = \frac{\mathbf{N}}{N} \times \mathbf{n} \quad (\text{A.10})$$

so that, after a little algebra

$$\varphi_N = \text{ArcXY}(\mathbf{n} \cdot \hat{\mathbf{M}}, \mathbf{m} \cdot \hat{\mathbf{M}}) \quad (\text{A.11})$$

$$\begin{aligned} &= \text{ArcXY} \left( \frac{(\mathbf{L} \times \mathbf{J})_{Z_Q}}{|\mathbf{L} \times \mathbf{J}|}, \frac{-NJ_{Z_Q}}{|\mathbf{L} \times \mathbf{J}|} \right) \\ &= \text{ArcXY} \left( \frac{-\sqrt{L^2 - L_{Z_Q}^2} \sqrt{J^2 - L_{Z_Q}^2} \sin \varphi_L^Q}{|\mathbf{L} \times \mathbf{J}|}, \frac{-NL_{Z_Q}}{|\mathbf{L} \times \mathbf{J}|} \right) \end{aligned} \quad (\text{A.12})$$

with

$$|\mathbf{L} \times \mathbf{J}|^2 = L^2 J^2 - \left( \frac{J^2 + L^2 - N^2}{2} \right)^2 \quad (\text{A.13})$$

That this is the correct definition of  $\varphi_N$  is checked by showing by mere derivation that  $dL_{Z_Q} \wedge d\varphi_L^Q = dN \wedge d\varphi_N$ .

Reciprocal relations are obtained from the right part of eq. (A.11)

$$L_{Z_Q} = -\frac{\sin \varphi_N}{N} |\mathbf{L} \times \mathbf{J}| \quad (\text{A.14})$$

and by extracting  $\cos \varphi_L^Q$  from eq. (A.8) and  $\sin \varphi_L^Q$  from the left part of eq. (A.11), and replacing  $L_{Z_Q}$  by the previous expression, which leads to:

$$\varphi_L^Q = \text{ArcXY} \left( \frac{N^2 - J^2 - L^2}{2} + \frac{\sin^2 \varphi_N}{N^2} |\mathbf{L} \times \mathbf{J}|^2, -\cos \varphi_N |\mathbf{L} \times \mathbf{J}| \right) \quad (\text{A.15})$$

## References

- [1] M. J. Seaton, Quantum defect theory, Rep. Prog. Phys. 46 (1983) 167–257.

- [2] U. Fano, Quantum defect theory of  $\ell$  uncoupling in  $H_2$  as an example of channel-interaction treatment, *Phys. Rev. A* 2 (2) (1970) 353.
- [3] U. Fano, Unified treatment of perturbed series, continuous spectra and collisions, *J. Opt. Soc. Am.* 65 (9) (1975) 979.
- [4] C. H. Greene, C. Jungen, Molecular applications of quantum defect theory, *Adv. At. Mol. Phys.* 21 (1985) 51.
- [5] C. Jungen (Ed.), *Molecular Applications of Quantum Defect Theory*, Institute of Physics Publishing (IOP), Bristol, 1996.
- [6] P. Labastie, M. C. Bordas, B. Tribollet, M. Broyer, Stroboscopic effect between electronic and nuclear motion in highly excited molecular Rydberg states, *Phys. Rev. Lett.* 52 (19) (1984) 1681–4.
- [7] M. C. Bordas, M. Broyer, J. Chevalyere, P. Labastie, S. Martin, Multichannel quantum defect theory analysis of the Rydberg spectrum of  $Na_2$ , *J. Phys.* 46 (1) (1985) 27–38.
- [8] M. Lombardi, P. Labastie, M. C. Bordas, M. Broyer, Molecular Rydberg states: classical chaos and its correspondence in quantum mechanics, *J. Chem. Phys.* 89 (6) (1988) 3479–90.
- [9] E. B. Bogomolny, Semiclassical quantization of multidimensional systems, *Comments At. Mol. Phys.* 25 (1-3) (1990) 67–81.
- [10] E. B. Bogomolny, Semiclassical quantization of multidimensional systems, *Nonlinearity* 5 (4) (1992) 805–66.
- [11] E. B. Bogomolny, On dynamical zeta function, *Chaos* 2 (1) (1992) 5–13.
- [12] T. Prosen, Quantum surface of section method: eigenstates and unitary quantum Poincaré evolution, *Physica D* 91 (1996) 244–77.
- [13] F. Leyvraz, R. A. Méndez-Sánchez, M. Lombardi, T. H. Seligman, Multichannel quantum defect theory: a quantum Poincaré map, *Phys. Lett. A* 268 (4-6) (2000) 309–14.
- [14] C. Jung, Poincaré map for scattering states, *J. Phys. A: Math. Gen.* 19 (8) (1986) 1345–53.
- [15] B. Dietz, M. Lombardi, T. H. Seligman, Parabolic manifolds in the scattering map and direct quantum processes, *J. Phys. A: Math. Gen.* 29 (5) (1996) L95–9.
- [16] T. Prosen, T. H. Seligman, H. A. Weidenmuller, Random matrix ensembles for semi-separable systems, *Europhys. Lett.* 55 (2001) 12.
- [17] M. Lombardi, T. H. Seligman, Universal and nonuniversal statistical properties of levels and intensities for chaotic Rydberg molecules, *Phys. Rev. A* 47 (5) (1993) 3571–86.
- [18] A. Messiah, *Mécanique Quantique*, Vol. 2, Dunod, Paris, 1964.

- [19] H. Goldstein, *Classical Mechanics*, 2nd Edition, Addison-Wesley Series in Physics, Addison-Wesley, Reading, MA, 1980.
- [20] L. D. Landau, E. M. Lifshitz, *Quantum Mechanics (Non-Relativistic Theory)*, 3rd Edition, Vol. 3 of *Course of Theoretical Physics*, Pergamon Press, Oxford, 1977.
- [21] F. Leyvraz, M. Lombardi, T. H. Seligman, A diffusion model for classical chaotic compound scattering, *Physica D: Nonlinear Phenomena* 157 (3) (2001) 169–85.
- [22] R. G. Hulet, D. Kleppner, Rydberg atoms in “Circular” states, *Phys. Rev. Lett.* 51 (16) (1983) 1430–3.
- [23] D. Delande, J. C. Gay, A new method for producing circular Rydberg states, *Europhys. Lett.* 5 (4) (1988) 303–8.
- [24] F. Benvenuto, G. Casati, D. L. Shepeliansky, Chaotic autoionisation of molecular Rydberg states, *Phys. Rev. Lett.* 72 (12) (1994) 1818–21.
- [25] R. Neuhauser, K. Siglow, H. J. Neusser, Hydrogenlike Rydberg electrons orbiting molecular clusters, *Phys. Rev. Lett.* 80 (23) (1998) 5089–92.
- [26] U. Even, R. D. Levine, R. Bersohn, Observations of molecular Rydberg state decay for  $n = 10$ –200, *J. Phys. Chem.* 98 (13) (1994) 3472–77.
- [27] M. V. Berry, Semi-classical mechanics of regular and irregular motion, in: G. Ioos, R. H. G. Helleman, R. Stora (Eds.), *Chaotic Behaviour of Deterministic Systems*, Vol. XXXVI of *Les Houches*, North-Holland, Amsterdam, 1983, Ch. 3, pp. 171–272.
- [28] M.-J. Giannoni, A. Voros, J. Zinn-Justin (Eds.), *Chaos and Quantum Physics*, Vol. LII of *Les Houches*, North-Holland, Amsterdam, 1991.
- [29] G. Herzberg, *Molecular Spectra and Molecular structure. I. Spectra of Diatomic Molecules*, 2nd Edition, Van Nostrand, New York, 1950.
- [30] K. Nakamura, Y. Okasaki, A. R. Bishop, Periodically pulsed spin dynamics: Scaling behavior of semiclassical wave functions, *Phys. Rev. Lett.* 57 (1) (1986) 5–8.
- [31] F. Haake, M. Kuś, R. Scharf, Classical and quantum chaos for a kicked top, *Z. Phys. B* 65 (1987) 381–95.
- [32] D. R. Hartree, *Proc. Camb. Phil. Soc.* 24 (1928) 426.
- [33] K. Husimi, *Proc. Phys. Soc. Japan* 22 (1940) 264.
- [34] E. P. Wigner, On the quantum correction for thermodynamic equilibrium, *Phys. Rev.* 40 (1932) 749–59.
- [35] A. R. Edmonds, *Angular Momentum in Quantum Mechanics*, 3rd Edition, Princeton University Press, Princeton, New Jersey, 1974.
- [36] G. Casati, G. Maspero, D. L. Shepelyansky, Quantum Poincaré recurrences, *Phys. Rev. Lett.* 82 (1999) 524–27.

- [37] H. Gräf, H. L. Harney, H. Längeler, C. H. Lewenkopf, C. Rangacharyulu, A. Richter, P. Schardt, H. A. Weidenmüller, Distribution of eigenmodes in a superconducting stadium billiard with chaotic dynamics, *Phys. Rev. Lett.* 69 (9) (1992) 1296–9.
- [38] W. H. Miller, Classical limit quantum mechanics and the theory of molecular collisions, *Adv. Chem. Phys.* 25 (1974) 69.